Research Square

Preprints are preliminary reports that have not undergone peer review.
They should not be considered conclusive, used to inform clinical practice,
or referenced by the media as validated information.

ACF7 promotes spontaneous metastasis in HER2-driven breast cancer through cytoskeletal coordination

Rebecca Cusseddu
Montreal Clinical Research Institute
Camille Malouf
Montreal Clinical Research Institute
Laura Quirion
Montreal Clinical Research Institute
Amélie Robert
Montreal Clinical Research Institute
Louis Gaboury
Institute for Research in Immunology and Cancer
Stéphanie Duhamel
Institut du cancer Rosalind & Morris Goodman
William J Muller
Institut du cancer Rosalind & Morris Goodman
Jean-François Côté
jean-francois.cote@ircm.qc.ca

Montreal Clinical Research Institute

Research Article

Keywords:

Posted Date: November 3rd, 2026

DOI: https://doi.org/10.21203/rs.3.rs-10553747/v1

License: This work is licensed under a Creative Commons Attribution 4.0 International License.
Read Full License

Additional Declarations: No competing interests reported.

ACF7 promotes spontaneous metastasis in HER2-driven breast cancer through cytoskeletal coordination

Rebecca Cusseddu[1,2], Camille Malouf[1], Laura Quirion[1,3], Amélie Robert[1], Louis Gaboury[4], Stéphanie Duhamel[5], William J Muller[5] and Jean-François Côté[1,2,3,6*]

[1]Montreal Clinical Research Institute (IRCM), Montreal, Canada.

[2]Department of Anatomy and Cell Biology, McGill University, Montreal, Canada.

[3]Molecular Biology Programs, Université de Montréal, Canada.

[4]Institute for Research in Immunology and Cancer (IRIC), Montreal, Canada.

[5]Goodman Cancer Institute, McGill University, Canada.

[6]Department of Medicine, Université de Montréal, Canada.

*Corresponding author:

Jean-François Côté, PhD

Montreal Clinical Research Institute (IRCM)

110 Pine Ave West

Montreal (Quebec) Canada

H2W 1R7

Email: jean-francois.cote@ircm.qc.ca

Phone: (514) 987-5647

This document file includes:

Abstract

Main Text

Figures 1 to 6

Supplemental information

Figures S1 to S5

Tables S1 to S5

Legends for Movies S1 to S5

References

Other supporting materials for this manuscript include the following

Movies S1 to S5

ABSTRACT

Background: Metastasis is the primary cause of breast cancer mortality, yet the cellular mechanisms that confer metastatic competence remain incompletely understood. Directed migration requires coordinated regulation of the actin and microtubule cytoskeletons, but how this integration contributes to metastatic progression *in vivo* remains unclear. Here, we investigated the role of ACF7, a spectraplakin that links actin filaments and microtubules downstream of HER2 signaling, in spontaneous metastasis of HER2-driven breast cancer.

Methods: We generated a genetically engineered mouse model combining HER2-driven mammary tumorigenesis with conditional loss of ACF7, enabling its contribution to spontaneous metastasis to be assessed in the context of primary tumor development. Primary tumor-derived cell lines were established and analyzed using live-cell imaging, immunofluorescence microscopy and three-dimensional spheroid assays to define the cellular mechanisms regulated by ACF7. Experimental metastasis models were used to examine its contribution to lung colonization, and its clinical relevance was evaluated in human breast cancer specimens and patient datasets.

Results: ACF7 loss markedly reduced spontaneous lung metastasis without affecting primary tumor burden or histopathological features. Mechanistically, ACF7 promoted cancer cell migration

and invasion by coordinating actin and microtubule organization, regulating microtubule dynamics and supporting focal adhesion maturation. These functions were conserved across independent HER2-driven tumor cell models. Experimental metastasis assays further demonstrated that ACF7 promotes lung colonization. In human breast tumors, ACF7 expression was elevated in HER2-positive cancers and associated with metastatic features and poorer patient survival.

Conclusions: ACF7 promotes spontaneous metastasis in HER2-driven breast cancer by coordinating actin-microtubule organization, microtubule dynamics and focal adhesion maturation, while remaining dispensable for primary tumor growth. These findings establish cytoskeletal coordination as a critical determinant of metastatic competence *in vivo* and identify ACF7-dependent cytoskeletal programs as potential metastasis-selective therapeutic vulnerabilities.

Keywords: ACF7, $HER2^{+}$ breast cancer, lung metastasis, cytoskeleton, migration.

INTRODUCTION

Breast cancer remains the most frequently diagnosed malignancy in women worldwide and a leading cause of cancer-related mortality, with most deaths resulting from metastatic rather than primary disease (1). Amplification or overexpression of human epidermal growth factor receptor 2 (HER2) occurs in approximately 15-20% of cases and is associated with an elevated risk of recurrence and distant metastasis (2-4). Although HER2-targeted therapies, including trastuzumab and pertuzumab, have significantly improved clinical outcomes (5-7), therapeutic resistance and metastatic relapse remain major clinical challenges (8-10). Defining the molecular and cellular mechanisms that enable tumors to metastasize therefore remains an important priority.

Metastasis is a highly inefficient multistep process in which tumor cells must acquire migratory and invasive properties, intravasate and survive into the circulation, and colonize distant tissues (11-14). Following dissemination, tumor cells may remain dormant for years, or alternatively undergo

rapid outgrowth, depending on both intrinsic and microenvironmental cues (15-17). While considerable progress has been made in identifying transcriptional programs such as epithelial-to-mesenchymal transition (EMT) that promote dissemination (18, 19), the cellular machinery that physically enables tumor cell movement and invasion remains ill-defined.

Directed cell migration requires precise spatial and temporal coordination of the filamentous actin (F-actin) and microtubule (MTs) networks. Together, these systems establish front-rear polarity, generate protrusive forces, and regulate adhesion dynamics (20-24). Actin polymerization drives membrane protrusions at the leading edge, while MTs contribute to cell polarity, intracellular trafficking, and focal adhesion turnover (25-28). Although actin and microtubule dynamics have been extensively characterized in cultured cells, how their coordination contributes to spontaneous metastatic progression downstream of oncogene signaling *in vivo* remains poorly understood.

The spectraplakin ACF7, also known as MACF1, is a large cytoskeletal crosslinker that physically couples F-actin and MTs, positioning it to integrate the two principal cytoskeletal systems governing directed migration (29-32). ACF7 promotes microtubule guidance along actin filaments toward focal adhesions, thereby supporting adhesion turnover and persistent cell migration. It has also been linked to Rac activation via its interaction with the ELMO/DOCK1 complex, while ubiquitin-dependent regulation of ACF7 stability modulates migratory and metastatic behavior (33-35). These properties position ACF7 at the interface between oncogenic signaling and the cytoskeletal machinery controlling cell movement.

During skin wound repair, localized inhibition of glycogen synthase kinase 3β (GSK3β) prevents phosphorylation-dependent dissociation of ACF7 from MTs, enabling MT capture along actin-rich protrusions and the establishment of front-rear polarity (29, 36, 37). A related signaling mechanism operates in breast cancer cells, where the HER2, Memo, RhoA, and mDia1 signaling pathway promotes localized GSK3β inhibition and adenomatous polyposis coli (APC)-mediated recruitment of ACF7 to the cell cortex (38-40). Cortical recruitment of ACF7 is required for MT capture and directional migration in response to HER2 signaling, and its depletion abolishes chemotactic responses (39). These studies established a mechanistic connection between HER2 and ACF7-

dependent migration in cultured cells, but whether ACF7 contributes to spontaneous HER-2 driven metastasis *in vivo* remains unknown.

Here, we address this question by conditionally deleting *ACF7* in a genetically engineered mouse model of HER2-driven mammary tumorigenesis, allowing its contribution to spontaneous metastasis to be evaluated in the context of primary tumor development. We show that ACF7 loss markedly reduces spontaneous lung metastasis without affecting primary tumor burden and histopathological features. Using primary tumor-derived cells and complementary *in vivo* models, we further demonstrate that ACF7 promotes metastatic progression by coordinating F-actin-MT organization, MT dynamics and focal adhesion remodeling. These findings establish ACF7-dependent cytoskeletal coordination as an important determinant of metastatic competence in HER2-driven breast cancer.

METHODS

Animal care and mouse strains

Mice used in this study were previously described: ACF7^{flx} mice (29), transgenic MMTV-NIC mice (MMTV-NeuNDL2-5-IRES-Cre) (41) and transgenic MMTV-Cre mice (42). All mice were backcrossed in FVB/NJ genetic background. Xenograft and tail-vein experiment were conducted in 6-week female nude mice (NU/J, 0020198; Jackson Laboratory). Mice were housed in a mouse-specific pathogen-free (SPF) facility. All animal experiments were conducted in accordance with protocols approved by the Institut de Recherches Cliniques de Montréal Animal Care Committee and complied with the Canadian Council of Animal Care rules (protocol 2020-14 COT). For transgenic mice, animals were monitored weekly by palpation for tumor development. According to the approved protocol, mice were euthanized five weeks after tumor onset to assess tumor initiation, tumor growth, and metastasis. This time-based endpoint constituted the maximum tumor burden permitted under the approved protocol. No animals exceeded the permitted tumor burden established, and no protocol deviations occurred with respect to tumor burden limits.

Whole-mount analysis of mammary gland development

Mammary gland-specific *ACF7* knockout mice were generated by crossing *MMTV-Cre* mice with *ACF7* $^{flx/flx}$ mice. Mammary glands number 9 were collected from 9-, 12- and 15-weeks old *MMTV-Cre*$^{+}$ *ACF7* $^{wt/wt}$ and *MMTV-Cre*$^{+}$ *ACF7* $^{flx/flx}$ and spread onto glass slide. Tissues were fixed overnight in 10% formalin, defatted by two successive overnight incubation in acetone, and stained overnight with carmine red solution (Sigma Aldrich). The glands were then processed in a graded ethanol series, cleared in xylene, and mounted using Permount (Fisher). Whole-mounts were imaged using a Car Zeiss Axiophot upright microscope (Carl Zeiss MicroImaging, Jena, Germany) equipped with ×2,5 objective, coupled to a Micropublisher camera (Q-Imaging, Houston, USA) and operated with Velocity software (Version #6.0). Mammary gland development was assessed by quantifying ductal branching as previously described in (43).

Tumor progression studies

A genetically engineered mouse model of ACF7 loss in HER2-driven mammary tumors was generated by crossing ACF7$^{flx/flx}$ mice with MMTV-NIC mice. Cohorts of 20 animals of NIC^{+}ACF7$^{wt/wt}$, NIC^{+}ACF7$^{wt/flx}$ and NIC^{+}ACF7$^{flx/flx}$ female mice were generated and monitored by regular palpation for mammary tumor development. Mice were sacrificed 5 weeks after detection of the first palpable tumor. The following measurements were taken on every mouse: analysis of the number of nodules, tumor mass, tumor volume, number of lungs metastasis and mammary intraepithelial neoplastic lesions (MINs). Tumor volume (in cm^3) was calculated as previously described in (44) using the formula [volume = 0,52 × (width)² × length]. Total tumor burden was calculated by summing the volume of all the tumors for each mouse, and similarly, the total tumor mass per mouse was determined. Tumors and lungs were collected and treated as described in the ***Histology and Immunohistochemical staining*** section. Imaging was performed using a Leica DM6 upright microscope (Leica, Wetzlar, Germany), equipped with ×40 objective, coupled to a DFC480 camera (Leica, Wetzlar, Germany) for acquisition of color images, operated with Las X software to acquire images; or a Leica DM4000B upright microscope (Leica, Wetzlar, Germany)

equipped with a ×5 and ×20 objectives, coupled with a DP72 camera (Olympus Corporation, Hachioji, Tokyo, Japan) and operated with OsteoMetrics software (OsteoMeasure7 v4.1.0.0).

Histology and Immunohistochemical staining

Tumors and lungs were collected, fixed, paraffin-embedded, and sectioned at a thickness of 5 µm for tumors and at 5 µm. For the analysis of lung metastases, serial sections were collected at 100 µm intervals. Sections were stained with hematoxylin and eosin (H&E) for histopathological analysis. For immunohistochemistry (IHC), tumor sections were deparaffinized in xylene and rehydrated through a graded ethanol series. Antigen retrieval was performed in 10mM sodium citrate buffer (pH6) according to standard procedures. Endogenous peroxidase activity was quenched with 3% H_2O_2, and sections were permeabilized in IHC buffer (0,5% Triton X-100 and 0,02% Tween-20 in PBS). After blocking with 1% bovine serum albumin in IHC buffer, sections were incubated overnight with the indicated primary antibodies (***Table S1***). Sections were then washed in IHC buffer and incubated with the appropriate biotinylated secondary antibody, followed by washes and incubation with streptavidin-HRP. After final washes, reaction was revealed using DAB peroxidase substrate kit (Vector Laboratories, SK-4100) and sections were counterstain with hematoxylin (Sigma-Aldrich).

Quantification of Mammary Intraepithelial Neoplastic Lesions (MINs)

Tumor free mammary gland number 4 or 9 from *MMTV-NIC*$^{+}$ *ACF7*$^{wt/wt}$, *MMTV-NIC*$^{+}$ *ACF7*$^{wt/flx}$ and *MMTV-NIC*$^{+}$ *ACF7*$^{flx/flx}$ mice were collected 5 weeks after tumor onset and mounted similarly as the whole-mount analysis section described above. The number of MINs was determined by counting the total amount of neoplastic lesions under a Carl Zeiss Axiophot upright microscope (Carl Zeiss MicroImaging, Jena, Germany) equipped with ×2,5 objective, coupled to a Micropublisher camera (Q-Imaging, Houston, USA) and operated with Velocity software (Version #6.0).

Western blot

Cell lysates were prepared in IGEPAL lysis buffer (150mM NaCl, 50mM Tris pH 7.5, 1% IGEPAL). For total tumor lysates preparation, nitrogen frozen tumors were lysed in Radio Immunoprecipitation Assay (RIPA) buffer (50 mM Tris pH 7.5, 0.1% SDS, 0.5% deoxycholic acid, 1% Nonidet P-40, 150 mM NaCl, 5 mM EDTA). Lysis buffers were supplemented with protease inhibitor (Sigma) and phosphatase inhibitors: 10 mM sodium fluoride (Sigma) and 1 mM sodium orthovanadate (Sigma). Protein concentration of each sample was determined using the BIO-RAD DC™ Protein Assay kit. Proteins were then denatured in 6X Laemmli loading buffer [5% SDS, 0.1 mM Tris pH 6.8, 140 mM β-mercaptoethanol, 25% glycerol] and boiled for 5 min at 95°C. Proteins were separated by SDS-PAGE and transferred to nitrocellulose before immunoblotting.

Antibodies, plasmids, shRNAs, primers, molecular cloning

The antibodies used in this study are presented in ***Table S1***, plasmids in ***Table S2***, shRNAs in ***Table S3*** and primers in ***Table S4***. ACF7 guide RNAs (gRNAs) listed in ***Table S5*** were designed using the online bioinformatics tool CHOPCHOP (https://chopchop.cbu.uib.no/) and subcloned into the BsmBI restriction enzyme sites of the plentiCRISPR v2 plasmid following an established protocol (45, 46). PL-EB3-EGFP was generated by subcloning EB3 from the EB3-GFP plasmid into the HindIII and BamHI restriction sites of PL-EGFP-C1.

Cell culture and stable cell lines generation

ACF7^{WT} and ACF7^{KO} cell lines were established from primary mammary tumors of *MMTV-NIC^{+}ACF7$^{wt/wt}$* and *MMTV-NIC^{+}ACF7$^{flx/flx}$* mice and kept in Dulbecco's modified Eagle's medium (DMEM, Wisent Bioproducts) supplemented with 5% fetal bovine serum (FBS, Wisent Bioproducts), 1% penicillin and streptomycin (P/S, Gibco) and MEGM SingleQuot Kit Suppl&Growth Factors (Lonza).

NMuMG-NeuNT cells, previously generated in (43), were cultured in DMEM supplemented with 10% FBS, 2mM L-glutamine (Gibco), 20mM Hepes pH 7,4 (Wisent Bioproducts), 10μg/mL insulin

and 1% P/S. HEK293T and HEK293FT cells lines were kept in DMEM supplemented with 10% FBS and 1% P/S. All cells were cultured at 37 °C and 5% CO_2.

To generate stable NMuMG-Neu-NT: shACF7 cell lines, lentiviral particles were produced in HEK 293FT cells by co-transfection of individual carrier pLKO.1 lentiviral plasmids (***Table S2***) with the packaging plasmids pRSV-Rev, pMDLg/pREE, and pMD2-VSVG. Transfections were performed with polyethyleneimine (PEI 25K™, Polysciences) at a ratio of 1µg DNA to 3µl PEI. At 48hours after transfection, virus containing supernatants were collected and passed through a 0.45 µm filter (Sarstedt). NMuMG-Neu-NT cells were infected with the filtered viral supernatants in the presence of 8 µg/mL polybrene (Sigma) for 16 hours. Transduced cells were subsequently selected with 1µg/mL puromycin (Wisent bioproducts) for 5 to 7 days. The resulting polyclonal populations were subjected to single-cell cloning, and individual clones were expanded and validated by immunoblotting.

To generate NMuMG-Neu-NT:ACF7-knockout cell lines, lentiviral particles encoding three independent ACF7-targeting gRNAs (mACF7 gRNA#2, #9 or #29) were produced separately in HEK293FT as described above. NMUMG-Neu-NT cells were co-infected for 16hours with lentiviruses encoding two different ACF7-targeting gRNAs and selected with 1µg/mL puromycin for 5 to 7 days. The resulting polyclonal populations were single-cell sorted by flow cytometry. Individual clones were expanded and screened for ACF7 loss by immunoblotting. Two independently generated clones were selected for subsequent experiments: $ACF7^{KO\#1}$, generated using mACF7-2 gRNA and mACF7-9 gRNA, and $ACF7^{KO\#2}$, generated using mACF7-9 gRNA and mACF7-29 gRNA.

To generate $ACF7^{WT}$ and $ACF7^{KO}$ cell lines stably expressing EB3-EGFP, retroviral particles were produced in HEK293T cells by co-transfection of the carrier pL-EGFP-EB3 retroviral plasmid with pCl-Ampho, and pMD2.G packaging plasmids as, described above. $ACF7^{WT}$ and $ACF7^{KO}$ cells were infected with EB3-EGFP-encoding retroviral particles for 16hours and subsequently selected using G418 for 5 days, at a concentration of 1,5 µg /mL for the WT cells and 2,5 µg/mL for the KO cells.

Live cell imaging

To monitor MT dynamics, ACF7^{WT}:EB3-EGFP and ACF7^{KO}:EB3-EGFP cells were seeded onto 18 mm coverslips (Fisher) coated with 5µg/ml fibronectin (Sigma, F2006) for 24 hours, prior to imaging using a Carl Zeiss Axio Observer Z1 motorized inverted microscope (Carl Zeiss MicroImaging, Jena, Germany) equipped with a Yokogawa CSU-X1 spinning-disk confocal head (Yokogawa Electric Corporation, Sugar Land, TX, USA), a Plan-Apochromat 63×/1.4 NA objective. Cells were maintained at 37˚C in 5% CO_2 during imaging using a Zeiss XLmulti S1stage-top incubator. Images were acquired every two seconds for a duration of two minutes. The resulting image sequences were processed using Fiji (version 2.14.0/1.54f).

For random migration assays, cells were seeded into 12-well plates pre-coated with 5µg/ml of fibronectin (Sigma, F2006) 24 hours prior to imaging. Time-lapse acquisition was performed using an IncuCyte microscope (Sartorius, version: 20192.2.0.0) equipped with a 10X objective, capturing images every hour for 24 hours. Cell migration was analyzed by manually tracking 40 cells per replicate using the Manual Tracking plugin in Fiji (version 2.14.0/1.54f). Quantification of migration parameters (directionality, velocity, and accumulated distance) was performed using the Chemotaxis Tool plugin in Fiji. For wound healing assays, cells were seeded into 12-well plates pre-coated with 5µg/mL fibronectin (Sigma, F2006) and cultured in DMEM with 10% FBS for 24 hours to reach a confluent monolayer. Cell monolayers were scratched using a 10 µL pipette tip, rinsed twice with PBS and fresh medium was added before imaging. Time-lapse images were acquired using the IncuCyte microscope (Sartorius, version: 20192.2.0.0) with a 4X objective, capturing images every hour for 24 hours. Migration was quantified by measuring the wound area using Fiji (version 2.14.0/1.54f).

Immunofluorescence (IF) staining

Before immunostaining, confluent cell monolayers were scratched as described above and allowed to migrate for 6 hours. For F-actin staining, cells were fixed 15 min at room temperature with 3.7% formaldehyde prepared in CSK buffer (100 mM NaCl, 300 mM sucrose, 3 mM $MgCl_2$, 10 mM

PIPES, pH 6.8). For tubulin staining, cells were fixed in ice-cold methanol for 5 min at -20C°. After fixation, cells were washed with PBS and permeabilized with 0,2% Triton-X100 in PBS for 5 min. Cells were then incubated with indicated primary antibodies (***Table S1***) diluted in wash buffer (1% BSA, 0.1% Triton-X100 in TBS). After washing, cells were incubated with the appropriate fluorescent secondary antibodies, with or without fluorescently-conjugated phalloidin, for 30 min at room temperature. Nuclei were counterstained with Hoechst for 10 minutes. Cells were extensively washed with wash buffer, once with distilled water, and mounted using Mowiol. Images were acquired with a Carl Zeiss LSM700 or LSM710 laser scanning confocal microscope (Carl Zeiss MicroImaging, Jena, Germany) equipped with a plan-apochromat ×63/1.4 numerical aperture objective and operated with ZenBlack 2009. Fiji (version 2.14.0/1.54f) was used for analyses.

Airyscan super-resolution microscopy

Cells were seeded onto 5µg/ml fibronectin-coated coverslips in 24-well plates and grown to confluence. Cell monolayer was scratched with a P20 pipette tip and allowed to migrate for 6hours before fixation with 0.5% glutaraldehyde and 2% formaldehyde in 0.1M sodium cacodylate pH 7.3. Free aldehydes were quenched by two successive 30 second incubations with 1% sodium borohydride in PBS. Immunostaining was performed in Wash buffer (TBS supplemented with 1% BSA, 0.1% Triton X-100). Super-resolution imaging was performed with a confocal laser scanning microscope ZEISS LSM 980 (Carl Zeiss AG, Oberkochen, Germany) equipped with an AiryScan2 detection unit. To maximize the resolution enhancement, high NA oil immersion alpha Plan-Apochromat 63X/1.40 Oil DIC M27 (Zeiss) was used. All imaging was performed using Immersol 518 F immersion media (n_e = 1.518 (23 °C); Carl Zeiss).

Invasion assay using spheroids

NIC tumor-derived and NMuMG-HER2 cells were maintained in their respective culture medium and harvested by trypsinization. Cells were counted using a TC20 Automated Cell Counter (Bio-Rad Cat#1450102), and 1000 cells were seeded per well in a Nunclon™ Sphera™ 96-Well, Nunclon Sphera-Treated, U-Shaped-Bottom Microplate (ThermoFisher Cat#174925). Plates were

centrifuged at 400g for 10 minutes at room temperature and incubated overnight at 37°C in a humidified 5% CO_2 incubator. The next day, collagen was added to each well at a final concentration of 3 µg/mL. Plates were centrifuged at 100g for 3 minutes at room temperature, and spheroids were cultured for an additional 6 days. Spheroids were transferred to the following embedding media: 1X DMEM (Sigma Cat#D2429), 8 mM NaOH, 0.375% $NaHCO_3$ (Gibco Cat#25080-094), 2 mM L-glutamine (Gibco Cat# 25030081), 10% FBS (MultiCell Cat#090150) and 1.5 mg/mL collagen I (Corning Cat#354249). Briefly, an ibidi 8-well chamber (ibidi Cat#80826) was covered with 100µL of the embedding media. Spheroids were then embedded in embedding media and transferred to pre-coated ibidi 8-well chamber slides and incubated at 37°C in a humidified atmosphere containing 5% CO_2 for 20 min to allow matrix polymerization. Following gelation, 100 µL of complete culture medium was carefully overlaid onto each well. Spheroid invasion was monitored by phase-contrast microscopy on a ZEISS Axio Observer 7 microscope. The extent of invasion was quantified as the area occupied by invading cells, calculated by subtracting the initial spheroid core area from the total spheroid area (core plus invading cells).

RNA extraction and RT- qPCR

Primers were designed using Primer3 (***Table S4***). RNA was extracted using the RNeasy Mini Kit (Qiagen), and reverse transcription was performed using 1 µg of total RNA with the TaqMan™ MicroRNA Reverse Transcription Kit (ThermoFisher). RT-qPCR was carried out using the PowerUp™ SYBR™ Green Master Mix (ThermoFisher) according to the manufacturer's instructions: 2 minutes at 50 °C, 10 minutes at 95 °C, followed by 40 cycles of 15 seconds at 95 °C and 1 minute at 60 °C, in a ViiA7-96 machine. The delta-CT were normalized using beta-actin levels.

Proliferation Assay

NMuMG-Neu-NT, or the $ACF7^{KO\#1}$, and $ACF7^{KO\#2}$ variant cells, were seeded at a density of 3000 cells per well in phenol reed-free DMEM (Wisent Bioproducts) 96-well plates, with triplicate wells per cell line and time point. Cell proliferation was assessed daily for 4 days using the CyQUANT

MTT Cell Proliferation Assay Kit (Invitrogen), according to the manufacturer's instructions. After solubilization and mixing by pipetting, absorbance was measured at 570 nm. Proliferation at each time was expressed relative to the absorbance measured on day 1.

Experimental lung metastasis by tail vein injection

NMuMG-Neu-NT, NMuMG-Neu-NT: ACF7$^{KO\#1}$ and NMuMG-Neu-NT: ACF7$^{KO\#2}$ cells (2 x 10^5) were resuspended in 200 µL of PBS were injected into the tail vein of 6-week-old nude mice using a 30G needle. Ten per were included per experimental group. At 30 days after injection, mice were sacrificed, and the lungs were harvested, perfused with formalin, and fixed overnight. Lungs were subsequently processed as described under the *Histology and Immunohistochemical staining* section above, sectioned, and stained with H&E. Histological sections were imaged using a Leica DM6 upright microscope, equipped with ×10 objective coupled with a DFC480 camera (Leica, Wetzlar, Germany). Las X software was used to acquire images. Metastatic burden was quantified using Fiji (version 2.14.0/1.54f) and expressed as the percentage of total lung tissue area occupied by metastatic lesions.

Human breast cancer tissue microarray analyses and ACF7 Immunohistochemical scoring

A cohort of 300 female breast cancer patients with tumors and various histological grades was used in this experiment. Formalin-fixed, paraffin-embedded (FFPE) samples containing tumor tissues were collected and prepared as tumor microarrays (TMA) at IRIC Histology core facility (Université de Montréal, Qc, Canada). Tumor grades were confirmed using Modified Scarff-Bloom-Richardson-Elston-Ellis (SBR-EE) grading system as describes in (47). Follow up data including the onset, metastasis and relapse were acquired. The Human Ethics Committee of the Université de Montréal Hospital Center approved the use of these specimens and research data (SL 05.019).

Immunohistochemical (IHC) staining of humans TMA was performed as described in Youssef et al. (47). IHC staining for ER, PR, HER2 and Ki-67 were used as surrogate markers to classify breast cancer tumors into luminal A, luminal B, HER-2 positive and triple negative breast cancer. TMA slides were stained and read blindly by two readers and scoring of ACF7 expression was assessed

using a two-tier scoring system described in (47). Briefly, the first parameter corresponds to the percentage of immunoreactive cells known as the quantity score (QS), estimated as follows: no staining was scored as 0, 1-10% of cells with positive staining were scored as 1, >10- 50% as 2, >50-70% as 3, and >70-100% as 4. The second parameter assesses the staining intensity score, rated as follows: no staining was scored as 0, weak staining as 1, moderate as 2 and strong staining as 3. The final product of the QS and staining intensity scores represent the total IHC Score that ranges from 0 to 12 (48, 49). IHC Scores between 0 and 4 represent low levels of expression while scores from >4 to 12 were considered as high levels of expression.

Transcriptomic analysis

Integration of The Genotype-Tissue Expression (GTEx) and the TCGA_BRCA datasets were performed as previously described in (50). The normalized mRNA expression z-scores relative to all samples of breast invasive carcinoma (TCGA, PanCancer Atlas, 2018) (n=1084) and Gtex (n=178) were downloaded from GTEX Portal (https://gtexportal.org/home/) and cBioPortal (https://www.cbioportal.org) (51-53).

RESULTS

ACF7 promotes spontaneous metastasis in a HER2-driven breast cancer model

Given the role of ACF7 in cytoskeletal organization downstream of HER2 signaling (38-40) in cultured cells, we investigated its contribution to HER2-driven mammary tumorigenesis and metastasis. Because global loss of *ACF7* is embryonic lethal (37), we first generated mice lacking ACF7 specifically in the mammary epithelium by crossing *ACF7*$^{flx/flx}$ mice with (54)-Cre mice. Whole-mount analyses of mammary glands collected at 9, 12, and 15 weeks of age revealed no differences in ductal outgrowth or branching between control and ACF7-deficient glands (Fig. S1A–D). Thus, ACF7 is dispensable for mammary gland development, allowing its function during tumor progression to be examined independently of developmental effects.

To examine the role of ACF7 in a HER2-driven model of breast cancer, ACF7$^{flx/flx}$ mice were crossed with MMTV-Neu-IRES-Cre (NIC) mice (41), which expresses an activated form of the HER2 rat ortholog (Neu) in the mammary epithelium (Fig. 1A). Female mice develop spontaneous mammary tumors, with lung metastases occurring in 60-80% of animals (Fig. S1E). Cohorts of NIC^{+}:*ACF7*$^{wt/wt}$, NIC^{+}:*ACF7*$^{wt/flx}$, and NIC^{+}:*ACF7*$^{flx/flx}$ mice (n= 20 per group) were monitored until 5 weeks after detection of the first palpable tumor. Immunoblotting confirmed the loss of ACF7 in tumors from NIC^{+}:*ACF7*$^{flx/flx}$ mice, without affecting Neu expression (Fig. 1B).

NIC^{+}:ACF7$^{flx/flx}$ mice exhibited a modestly earlier tumor onset than control animals (Fig. 1C). Despite this difference in latency, *ACF7* loss had no measurable impact on primary tumor burden at endpoint, as both number of tumors and total tumor masses were comparable across genotypes (Fig. 1D and E), with no differences in tumor size distribution (Fig. S1F). *ACF7* deletion also did not alter the number of mammary intraepithelial neoplastic (MINs) lesions (Fig. 1F and G), tumor adenocarcinoma histopathology (Fig. 1H), or tumor cell proliferation, as assessed by Ki67 staining (Fig. S1G and H). These findings indicate that ACF7 is not required for primary tumor growth in this model.

In contrast, *ACF7* loss markedly decreased spontaneous lung metastasis. Although lung metastases occurred in all three genotypes (Fig. 1I), NIC^{+}:*ACF7*$^{flx/flx}$ mice developed more than two-fold fewer metastatic lesions than NIC^{+}:*ACF7*$^{wt/wt}$ animals (Fig. 1J). Metastatic burden was comparable between NIC+:*ACF7*$^{wt/wt}$ and NIC+:*ACF7*$^{wt/flx}$ mice, indicating that retention of one functional allele of *ACF7* was sufficient to preserve metastatic capacity. Collectively, these results establish ACF7 as a selective promoter of spontaneous metastasis in HER2-driven breast cancer, with no detectable contribution to primary tumor growth after tumor onset.

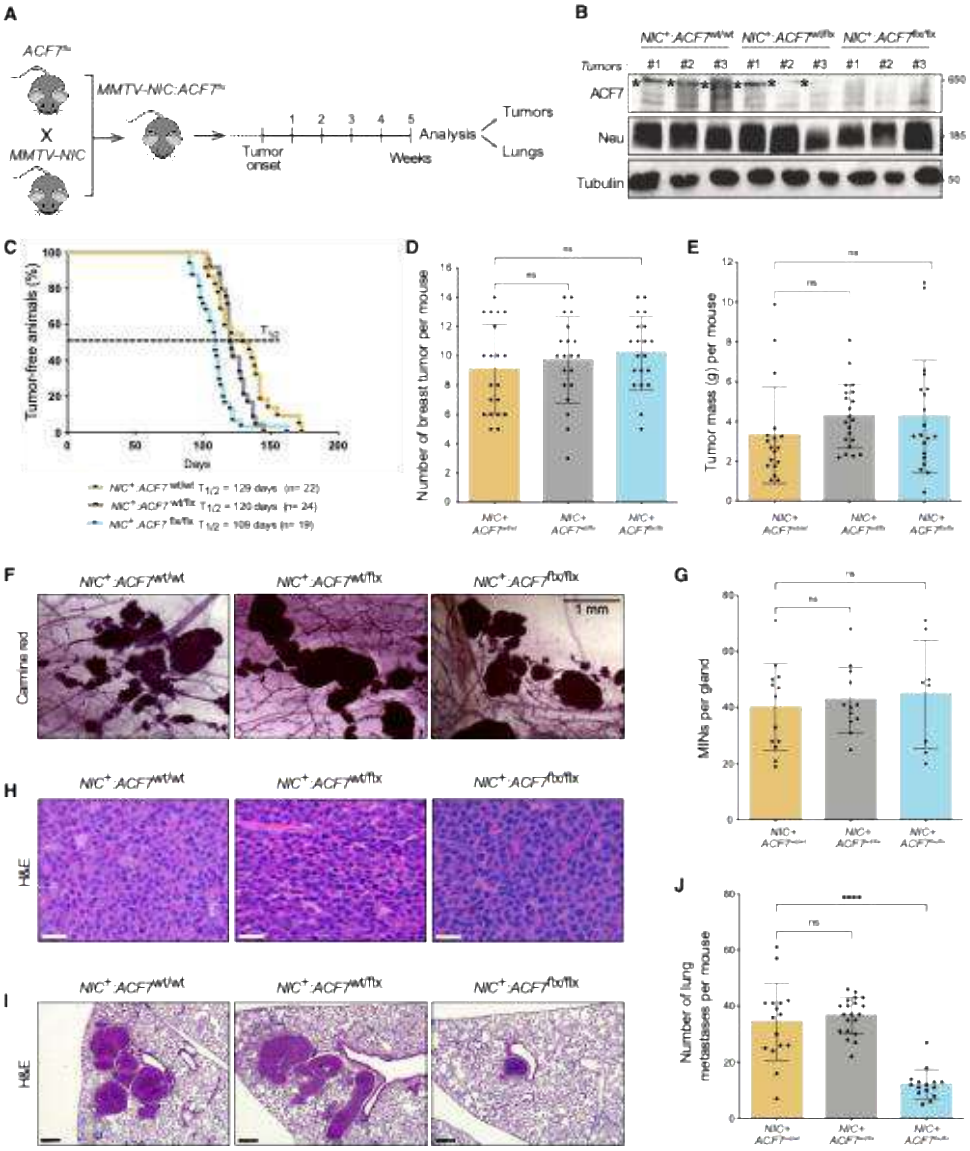
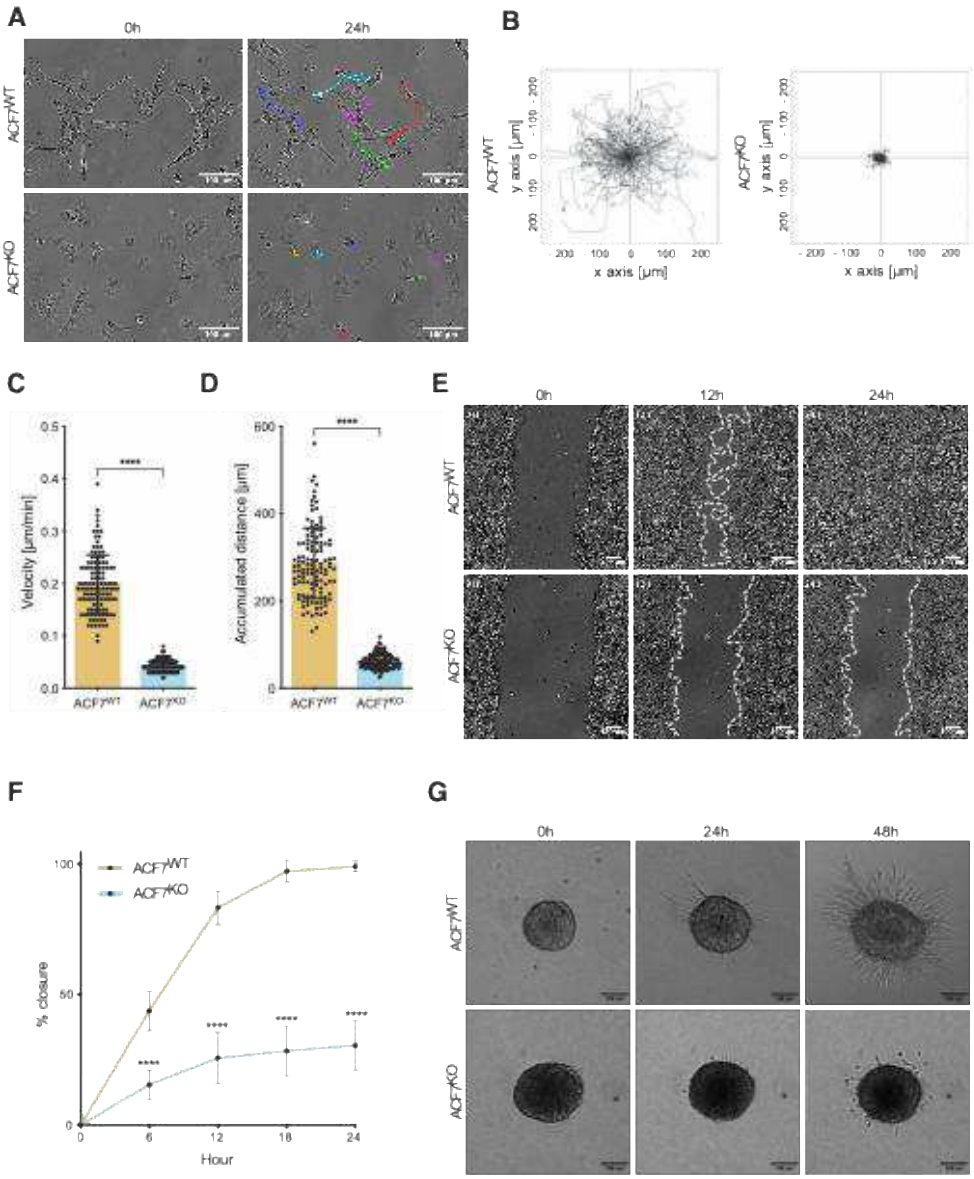


Fig 1. ACF7 loss reduces lung metastasis without impairing primary tumor growth in HER2-driven breast cancer. A) Experimental design: *ACF7*$^{flx/flx}$ mice were crossed with *MMTV-NIC* mice to generate NIC^{+}:*ACF7*$^{wt/wt}$, NIC^{+}:*ACF7*$^{wt/flx}$, and NIC^{+}:*ACF7*$^{flx/flx}$ mice. These mice were sacrificed 5 weeks after the detection of the first palpable tumor, and tumors and lungs were collected for analysis. **B)** Immunoblot analysis of ACF7, Neu and tubulin three different tumors per genotype. The ACF7 band is indicated by an asterisk and tubulin was used as a loading control. Data representative of three independent experiments. **C)** Kaplan-Meier analysis of tumor onset (n=20-24 mice per genotype). **D)** Number of mammary tumor nodules per mouse at endpoint (n=19-24

mice per genotype). **E)** Total tumor mass per mouse at endpoint (n=19-24 mice per genotype). **F)** Representative carmine-stained whole-mounts of tumor-free mammary glands showing mammary intraepithelial neoplastic (MINs) lesions (55). Scale bar: 1 mm, 2,5X. **G)** Number of MINs lesions per tumor-free inguinal mammary glands (n=7-17 mice per genotype). **H)** Representative H&E-stained sections of mammary tumors 5 weeks after detection of the first palpable tumor. Scale bar: 100 µm, 20X. **I)** Representative H&E-stained sections of lungs collected at endpoint. Metastatic lesions appear purple. Scale bar: 800 µm, 5X. **J)** Number of spontaneous lungs metastases per mouse (n=15-20). The data in **D, E, G** and **J** are presented as mean ± SD, and statistical analysis was performed using one-way ANOVA, $^{****}p = <0.0001$.

ACF7 promotes cancer cell motility and invasion.

To define the cellular mechanisms underlying the reduced metastatic burden caused by *ACF7* loss, we established primary tumor-derived cell lines from NIC^{+}:*ACF7*$^{wt/wt}$ and NIC^{+}:*ACF7*$^{flx/flx}$ mammary tumors, hereafter referred to as ACF7^{WT} and ACF7^{KO}, respectively. ACF7 deletion was confirmed by genomic DNA PCR and at the protein level by immunoblotting (Fig. S2 A-B). We first examined random cell motility on fibronectin-coated surfaces. Live-cell tracking revealed that ACF7^{KO} cells migrated more slowly and covered a shorter cumulative distance that ACF7^{WT} cells (Fig. 2 A-D, Movie S1). ACF7 loss similarly impaired migration in scratch-wound assays performed on fibronectin matrix, as reflected by reduced wound closure by ACF7^{KO} cells (Fig. 2E and F, Movie S2). We next assessed invasive capacity in 3D collagen matrix. After 48hours, ACF7^{KO} spheroids displayed less invasive outgrowth than ACF7^{WT} spheroids, resulting in a significant reduction in invasion area (Fig. 2G; Fig. S2C). Notably, the spheroid core area was comparable between genotypes, indicating that the reduced invasive area did not result from impaired spheroid formation or growth (Fig. S2D). Together, these results demonstrate that ACF7 promotes both tumor cell motility and invasion. These cellular defects provide a mechanistic basis for the reduced spontaneous metastatic burden observed following ACF7 deletion in the MMTV-NIC model.



418

419 **Fig 2. ACF7 promotes motility and invasive outgrowth of HER2-driven tumor cells. A-D)**
420 Random migration of ACF7^{WT} and ACF7^{KO} MMTV-NIC tumor-derived cells on fibronectin. Individual
421 cells were tracked at 1hour intervals for 24hours, with 40 cells analyzed per independent
422 experiment (n=3). **A)** Representative phase contrast images of the same field at the beginning and
423 end of the experiment. Colored tracks represent the trajectories of individual cells over 24hours.
424 Scale bar: 100 µm. **B)** Wind-rose plots represent the directional movement of individual MMTV-NIC
425 tumor-derived cells. **C)** Graph shows the cell velocity in µm/min. **D)** Graph shows the total distance
426 traveled by cells in µm. **E)** Representative phase-contrast images of ACF7^{WT} and ACF7^{KO} cell

monolayers at the indicated time after wound. Scale bar: 100 μm. **F)** Quantification of wound closure percentage every 6 hours for 24 hours (n=3). **G)** Representative phase contrast images of spheroids after 48 hours in collagen. Scale bars, 100 μm. The data in **C** and **D** are presented as mean ± SD, with statistical analysis performed using a t-test, and data in **F** are presented as mean ± SD, with statistical analysis performed using two-way ANOVA, **** $p < 0.0001$.

ACF7 coordinates cytoskeletal organization and microtubule dynamics to during cell migration

Because ACF7 physically link F-actin and MTs, we examined how its loss affects cytoskeletal organization during directed migration. Following scratch-induced migration, $ACF7^{WT}$ cells displayed coordinated orientation of the F-actin and MT networks toward the leading edge, with both networks extending into the leading-edge protrusions (Fig. 3A). In contrast, $ACF7^{KO}$ cells displayed cytoskeletal disorganization. MTs appeared straighter and failed to conform to the organization of the actin network, while F-actin accumulated toward the rear of the cell. Consequently, both cytoskeletal networks shoed reduced extension toward the leading edge (Fig. 3A). Because microtubule targeting of focal adhesions contributes to adhesion turnover during migration (56), we next examined adhesion organization by staining for paxillin. $ACF7^{KO}$ cells exhibited enlarged focal adhesions compared to $ACF7^{WT}$ cells (Fig. 3B and C). This phenotype is consistent with impaired focal adhesion turnover and provides some insights to explain the reduced migratory capacity of ACF7-null cells.

We next examined MT acetylation, a feature associated with long-lived MTs (57-59). In migrating $ACF7^{WT}$ cells, acetylated MTs (anti-acetylated lysine 40 of α-tubulin) formed elongated, curved tracks that extend from the perinuclear region toward the cell periphery (Fig. 3D). In $ACF7^{KO}$ cells, acetylated α-tubulin staining was predominantly punctate and confined to the perinuclear region. The straighter MTs extending toward the leading edge showed little or no detectable acetylation, indicating a loss of spatially organize MT acetylation in migrating cells (Fig. 3D). Consistent with these observations, immunoblotting revealed a substantial reduction in the ration of acetylated α-

455 tubulin over total α-tubulin in ACF7^{KO} cells (Fig. 3E). Finally, we monitored MT plus-end dynamics
456 in living cells using EB3-EGFP (60). In ACF7^{WT} cells, EB3-labeled plus-ends underwent persistent
457 and directional growth toward the cell cortex. By contrast, EB3-tracks in ACF7^{KO} cells were shorter
458 and less directionally organised, consistent with reduced MT growth persistence (Fig. 3F, Movie
459 S3). Together, these findings demonstrate that ACF7 coordinates F-actin and MTs organization,
460 maintains spatially polarized MT acetylation, and support persistent MT growth during migration.

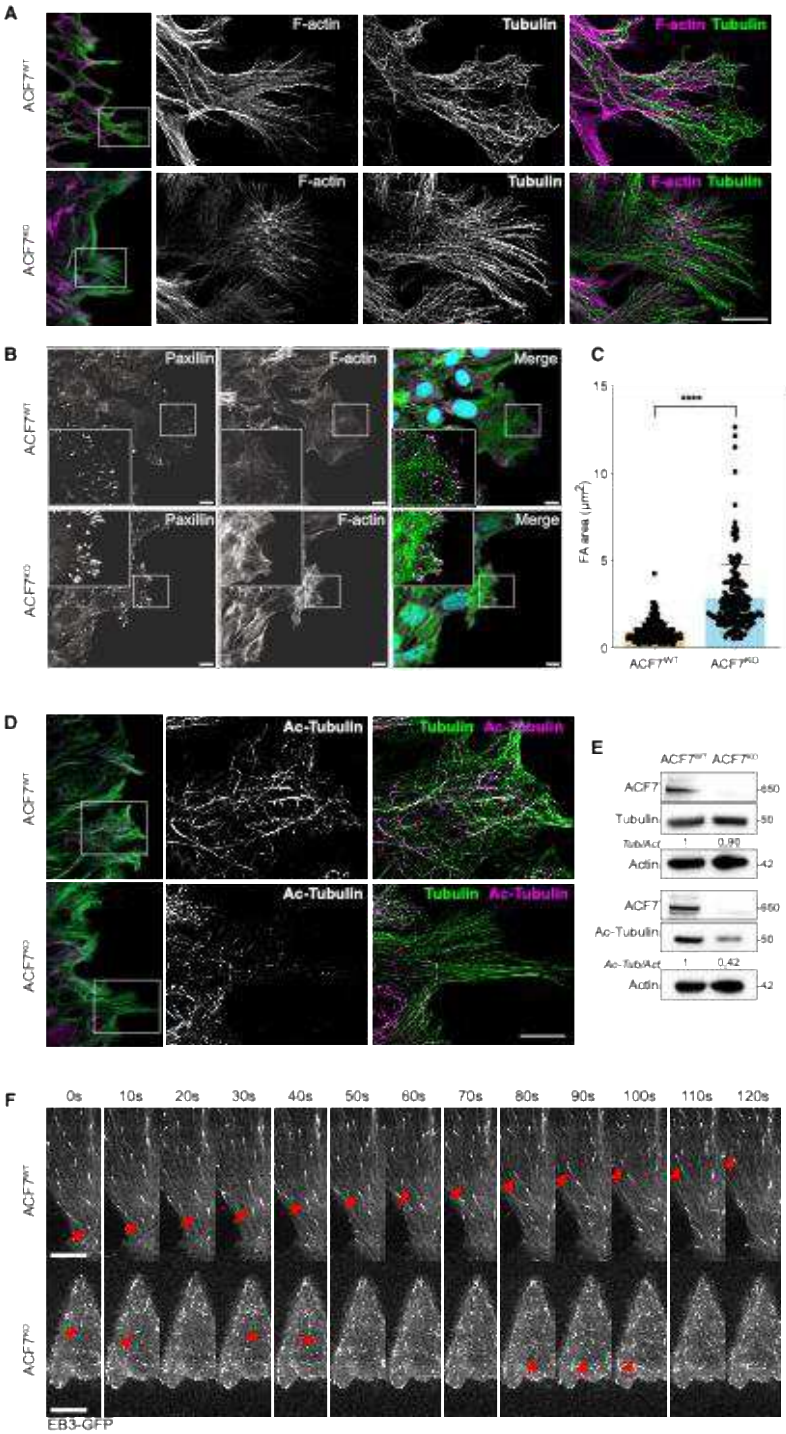


Fig 3. ACF7 coordinates cytoskeletal organization during tumor cell migration. A) Representative Airyscan super-resolution images of α-tubulin and F-actin in ACF7^{WT} and ACF7^{KO} cells 6 hours after wounding. Enlarged regions highlight differences in F-actin and MTs organization at the leading edge. Scale bar: 10 μm. **B)** Representative immunofluorescence images of paxillin

(magenta), F-actin visualized with phalloidin (green), and nuclei stained with DAPI (cyan), 6hours after scratch wounding. Scale bar: 10 µm. (n=3, N=30). **C)** Mean focal adhesion area in $ACF7^{WT}$ and $ACF7^{KO}$ (μm^2 ± SD, n=3, N=195 focal adhesion), with statistical analysis performed using a t-test, **** $p < 0.0001$. **D)** Representative super-resolution images of acetylated Tubulin on Lys40 (Ac-Tubulin) and total tubulin co-staining performed 6 hours after scratch wounding. Enlarged regions emphasize the continuous acetylation of flexible microtubules in $ACF7^{WT}$ versus $ACF7^{KO}$ cells. Scale bar: 10µm. **E)** Western blot comparing the acetyl modification of tubulin in $ACF7^{WT}$ and $ACF7^{KO}$ cells (n=3). The ratio is established based on actin expression, which is comparable between the cell lines. **F)** Representative timelapse images of real-time tracking of growing MTs with the marker EB3-EGFP. Red arrows follow the growing ends of individual microtubules. Scale bar: 10 µm (n=3).

ACF7 promotes motility and invasion in an independent HER2-driven cellular model

To determine whether the functions of ACF7 were conserved in an independent HER2-driven model, we used NMuMG mammary epithelial cells transformed with activated Neu (NMuMG-Neu-NT) (61). We initially depleted ACF7 using shRNA and confirmed reduced ACF7 expression by immunoblotting (Fig. S3A). ACF7-depleted clones exhibited reduced wound closure compared to control cells, reproducing, although less prominently, the migration defects observed in NIC tumor-derived cells (Fig. S3B and C, Movie S4).

We next generated $ACF7^{KO}$ cell lines using CRISPR/Cas9. Two independent clones ($ACF7^{KO\#1}$ and $ACF7^{KO\#2}$) lacked detectable ACF7 expression at both the protein and transcript levels, without affecting Neu expression (Fig. 4A, Fig. S4A and B). Both $ACF7^{KO\#1}$ and $ACF7^{KO\#2}$ clones demonstrated delayed migration in scratch-wound assays, confirming that ACF7 promotes motility in NMuMG-Neu-NT cells (Fig. 4B and C, Movie S5). ACF7 loss also impaired invasive outgrowth in 3D collagen matrix. ACF7 loss also impaired outgrowth in 3D collagen matrix. After 48 h, spheroids formed by both $ACF7^{KO}$ clones showed significantly reduced invasive structures and a reduced invasion area compared with control spheroids (Fig. 4D and E). The spheroid core area was unchanged in $ACF7^{KO\#1}$ cells but was modestly decreased in $ACF7^{KO\#2}$ cells (Fig. 4F).

Nevertheless, both clones displayed a consistent reduction in invasive outgrowth, whereas ACF7 loss did not affect proliferation under two-dimensional culture conditions (Fig. S4C). These results support a role for ACF7 in invasion. Finally, we next examined cytoskeletal organization during scratch-induced migration. In control cells, F-actin and MTs were coordinately oriented toward the wound edge. By contrast, both ACF7^{KO} clones showed disorganization of the actin and MT networks, with reduced alignment toward the direction of migration (Fig. 4G). Thus, complementary shRNA and CRISPR/CAS9 approaches in an independent HER2-driven model confirm that ACF7 promotes cytoskeletal organization, cell migration, and invasion.

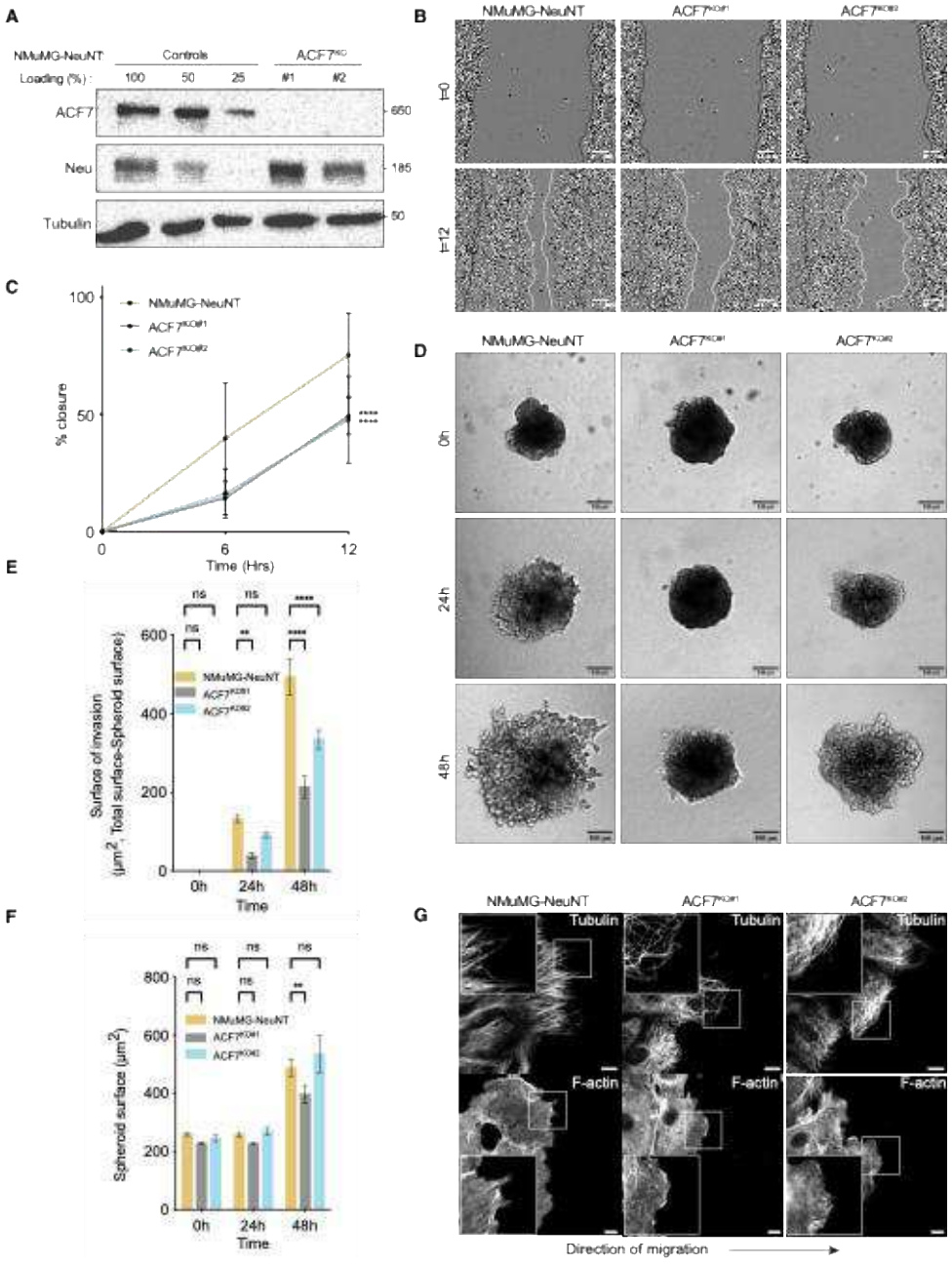
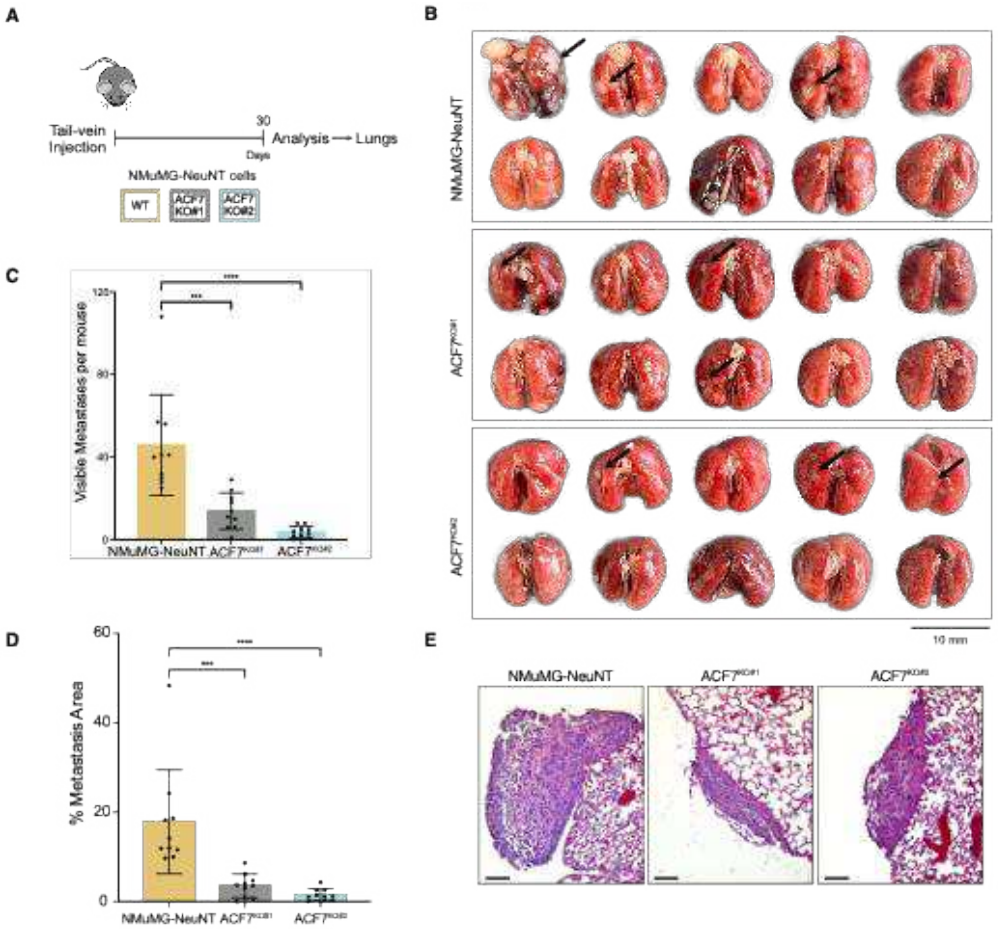


Fig 4. ACF7 is required for migration, invasion and cytoskeletal organization in NMuMG-Neu-NT cells. A) Immunoblot confirming the absence of ACF7 and the presence of Neu in two CRISPR/Cas9-edited clones targeting *ACF7*. α-Tubulin was used as loading control. **B)** Representative images of the indicated NMuMG-Neu cell monolayers at 0 and 12 hours after wound. Scale bar, 100 µm. **C)** Quantification of the wound closure (%) after 12 hours of migration (n=3). **D)** Phase contrast images of typical spheroids after 48 hours days in collagen. Scale bars,

100 µm. **E)** Graph shows the surface of invasion per spheroids at 0, 24 and 48hours. **F)** Graph shows the spheroid surface at 0, 24 and 48hours. **G)** Immunofluorescence images for tubulin and phalloidin staining, showing MTs and actin filaments, respectively, 6 hours after a wound-scratch induced migration. Scale bar: 10 µm. (n=3, N=30). Data are presented as mean ± SD (**C**) or ± SEM (**E and F**). Statistical analyses were performed using one-way ANOVA **(C)** or two-way ANOVA (**E and F**), with significance indicated as **p<0,01, ***p <0,001 ****p < 0.0001.

ACF7 promotes metastatic dissemination *in vivo*.

To determine whether ACF7 contributes to lung metastasis, we injected NMuMG-Neu-NT control cells or ACF7$^{KO\#1}$ and ACF7$^{KO\#2}$ cells into the tail veins of recipient mice, thereby bypassing escape from the primary tumor and intravasation (Fig. 5A). Lungs were collected and analyzed thirty days after injection. Although visible lung metastases developed in all groups, mice injected with either ACF7^{KO} clones developed fewer metastatic lesions than mice injected with control cells (Fig. 5B and C). Further histological analyses revealed a marked reduction in metastasis burden, with ACF7-null cells showed metastases occupying a substantially smaller fraction of lung area (Fig. 5D-E). Thus, ACF7 loss consistently impaired lung metastatic burden in two independent knockout clones, demonstrating that ACF7 promotes one or more post-intravasation steps required for efficient lung colonization *in vivo*.



527

528 **Fig 5. ACF7 loss reduces experimental lung metastasis of NMuMG-Neu-NT cells. A)**
529 Experimental design: NMuMG-Neu-NT, ACF7$^{KO\#1}$, and ACF7$^{KO\#2}$ cells were injected into the tail
530 veins of nude mice, N=10 per condition. Lungs were collected for analysis 30 days post-injection.
531 **B)** Representative images of the lungs 30 days post-injection. Black arrows highlight representative
532 examples of visible metastases. Scale bar, 10 mm. **C)** Quantification of the number of visible
533 metastases on whole lungs. **D)** Quantification of metastatic area (%) in the lungs based on
534 histological sections covering the entire lung. **E)** Histological H&E staining images of tumors five
535 weeks after injection into the mammary gland. Scale bar, 100 µm. Data are presented as mean ±
536 SD **(C, D)** Statistical analyses were performed using one-way ANOVA (**D)** or two-way ANOVA **(C)**,
537 with significance indicated as ***p <0,001, ****p < 0.0001.

538

539

ACF7 protein is elevated in HER2-positive breast tumors and associates with metastatic disease

To explore the clinical relevance of our experimental findings, we examined ACF7 expression in human breast cancer tumors. Immunohistochemical analysis was performed on a tissue microarray (TMA) comprising 310 breast tumor specimens with associated clinical annotation (Fig. S5A). Tumors were classified into surrogate breast cancer subtypes based on estrogen receptor (ER), progesterone receptor (PR), HER2, and Ki67 status (47). ACF7 protein was broadly detected across all subtypes but was expressed at the highest in HER2-positive tumors (Fig. 6A and B). We next analyzed *ACF7* transcript abundance across breast cancer subtypes using The Cancer Genome Atlas (TCGA) dataset. In contrast to the protein level differences observed by immunohistochemistry, *ACF7* mRNA levels did not differ significantly among subtypes (Fig. S5B). This discordance suggests that the elevated ACF7 protein expression observed in HER2-positive tumors may involve post-transcriptional regulation, although differences between cohorts and analytical platforms cannot be excluded. We then examined the relationship between ACF7 protein expression and metastatic features in patients of our cohort with available clinical follow-up. High ACF7 expression was associated with more frequent lymph node involvement and a greater proportion of patients who developed distant metastases, including metastases to the bone, liver, lung, and brain (Fig. 6C). Together, these findings indicate that ACF7 is expressed in HER2-positive breast tumors and suggest an association with metastatic progression in patients, consistent with its functional role in promoting metastasis in experimental models.

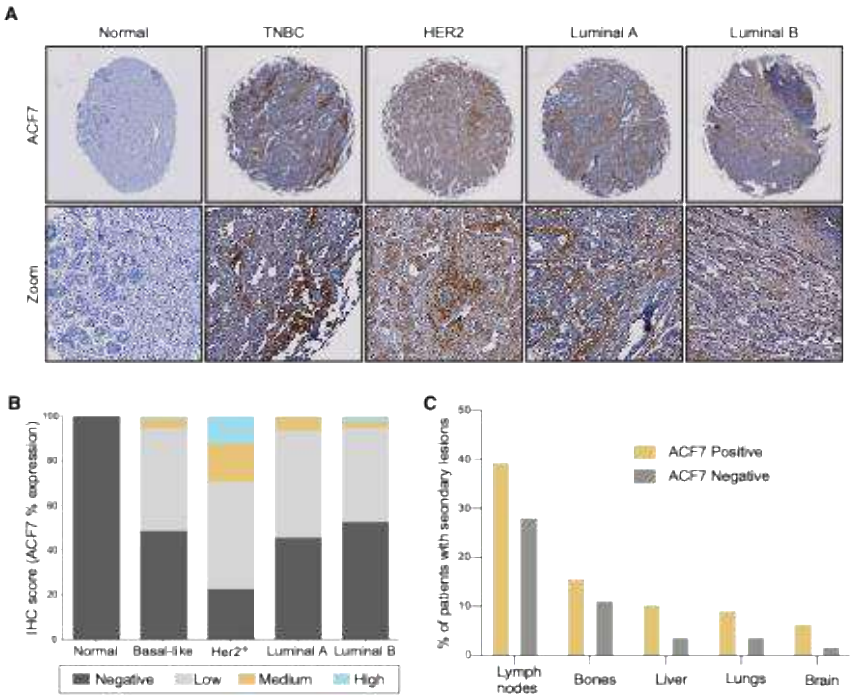


Fig 6. ACF7 is expressed in HER2+ breast cancer tumors and is associated with metastatic disease. A) Representative immunohistochemical staining showing ACF7 expression across different breast cancer subtypes. **B)** Distribution of ACF7 IHC scores calculated from patients' tissue samples in the TMA cohort, divided by the different subtypes and stratified into low, medium, or high scores (see ***methods*** for details). **C)** Percentage of patients who developed metastases at the indicated secondary sites, stratified according to ACF7 expression. Clinical follow-up data was available for 129 patients.

DISCUSSION

Metastasis remains the principal cause of mortality in breast cancer. Despite its clinical importance, the cellular mechanisms that enable tumor cells to disseminate and colonize distant organs remain incompletely understood (12). Our study identifies ACF7 as an important determinant of spontaneous metastasis in HER2-driven breast cancer. Conditional deletion of *ACF7* in the MMTV-NIC model markedly reduced lung metastasis without impairing primary tumor growth, histopathology, or proliferation after tumor onset. This separation between primary tumor burden

and metastatic capacity is a central finding of the study that establishes ACF7 as a metastasis-specific cytoskeletal organizer that is needed for metastatic competence *in vivo*.

Previous work from our laboratory began implicating ACF7 in breast cancer cell plasticity and metastasis. In an shRNA screen targeting microtubule plus-end tracking proteins in MDA-MB-231 cells, a cell line derived from triple-negative breast cancer, we identified ACF7 as a regulator of migration and epithelial-to-mesenchymal transition (35). The E3 ubiquitin ligase HectD1 was established as a post-translational regulator of ACF7. HectD1 promoted ACF7 ubiquitination and proteasomal degradation, whereas HectD1 depletion stabilized ACF7 and enhanced EMT, migration, and metastasis (35). A separate body of cellular work provided a compelling rationale for us to investigate the contributions of ACF7 in HER2-driven breast cancer in this study. HER2/ErbB2 signaling was shown to regulate microtubule capture and directional migration through Memo, RhoA, and mDia1, together with localized inhibition of GSK3β and APC-dependent recruitment of ACF7 to the cell cortex (38-40). These studies established a mechanistic link between HER2 activation and ACF7-dependent cytoskeletal remodeling but were restricted to cultured cells. The present work closes this important gap by demonstrating genetically that ACF7 contributes to spontaneous metastasis in an autochthonous HER2-driven tumor model. Thus, whereas the HectD1 study established that ACF7 abundance can regulate metastatic behavior, the current study places ACF7 within a defined oncogenic context and demonstrates the *in vivo* importance of the HER2-ACF7 cytoskeletal axis.

A central finding of this study is the dissociation between primary tumor growth and metastatic progression upon *ACF7* loss *in vivo*. In a genetically engineered HER2-driven model that recapitulates spontaneous tumor development and lung metastasis, deletion of *ACF7* did not affect tumor burden, histopathology, or proliferation, yet significantly reduced metastatic burdens. This is notable given that several MT-plus-end tracking proteins (+TIPs) that functionally associate with ACF7, including EB1-family proteins, are essential for cell division through their roles in mitotic spindle organization and microtubule capture (62). In contrast, our findings indicate that ACF7 is not required for proliferative capacity but instead governs the spatial organization of microtubules

toward the leading edge of migrating breast cancer cells. This selective phenotype indicates that the cellular machinery required for tumor expansion can be uncoupled from that enabling dissemination and colonization. Conceptually, these data suggest that metastasis relies on specialized cellular functions beyond those driving proliferation. In this context, ACF7 is defines as a regulator that is not broadly required for tumor growth but becomes critical when tumor cells engage in the metastatic cascade.

Our cellular findings provide a mechanistic basis for this metastatic phenotype. Across primary NIC tumor-derived cells and an independent NMuMG-Neu-NT model, ACF7 loss impaired migration and invasion and disrupted the coordinated orientation of F-actin and microtubules toward the leading edge. ACF7-deficient cells also displayed enlarged focal adhesions, reduced α-tubulin acetylation, and less persistent and directional EB3-positive microtubule growth. These observations are consistent with the established function of ACF7 in guiding microtubules along actin filaments toward peripheral adhesions, thereby supporting cytoskeletal polarity and adhesion remodeling (29, 30, 36). Because the present experiments do not directly measure focal adhesion turnover, the enlarged adhesions should be interpreted as consistent with impaired remodeling rather than as direct evidence of reduced turnover. Similarly, reduced tubulin acetylation indicates a loss of long-lived, spatially organized microtubules but does not by itself establish a causal role for acetylation in the metastatic phenotype.

The complementary *in vivo* models suggest that ACF7 contributes to more than one component of the metastatic cascade. The MMTV-NIC model captures spontaneous progression from a primary mammary tumor to lung metastasis and therefore provides the strongest evidence that ACF7 promotes metastasis in its native tumor context. Tail-vein injection bypasses local invasion and intravasation but still requires tumor cells to survive in the circulation, arrest within the lung vasculature, extravasate, survive in the lung microenvironment, and undergo metastatic outgrowth. The reduction in metastatic burden produced by two independent ACF7-knockout clones therefore supports a role for ACF7 in one or more post-intravasation steps required for efficient lung colonization. Further studies will be needed to determine whether ACF7 primarily controls early

dissemination, extravasation, survival at the secondary site, metastatic outgrowth, or several of these processes.

Together, our findings establish that cytoskeletal integration is not simply a correlate of aggressive tumor behavior but a functional requirement for efficient metastasis in HER2-driven breast cancer. They also identify ACF7 as a point of convergence between oncogenic signaling and the physical machinery of tumor cell migration. Because ACF7 has important physiological functions and was not pharmacologically targeted here, its therapeutic potential remains to be established. Nevertheless, defining the signaling and regulatory mechanisms that control ACF7 localization, stability, and activity may reveal more tractable approaches to disrupt metastatic competence while limiting effects on primary tumor growth.

CONCLUSION

In summary, this study provides genetic evidence that ACF7 promotes spontaneous metastasis in HER2-driven breast cancer while remaining dispensable for the growth of established primary tumors. ACF7 supports metastatic competence by coordinating actin and microtubule organization, persistent microtubule growth, and focal adhesion architecture during tumor cell migration and invasion. By extending the previously defined HER2-ACF7 signaling mechanism from cultured cells to spontaneous metastasis *in vivo*, these findings establish cytoskeletal coordination as an important determinant of HER2-driven metastatic progression.

Abbreviations

ACF7	Actin Cross-Linking Family Protein 7 (also known as MACF1)
DOCK1	Dedicator of Cytokinesis 1
EB1	End-Binding 1 protein
EB3	End-Binding 3 protein
ELMO	Engulfment and cell motility
EMT	Epithelial-to-mesenchymal transition

F-actin	Filamentous actin
GSK3β	Glycogen synthase kinase 3β
HectD1	HECT Domain E3 Ubiquitin Protein Ligase 1
HER2	Human epidermal growth factor receptor 2 (also known as ErbB2)
Ki67	Antigen Kiel 67
MACF1	Microtubule Actin Crosslinking Factor 1 (also known as ACF7)
mDia1	Diaphanous related formin-1
Memo	Mediator of cell motility 1
MINs	Mammary Intraepithelial Neoplastic Lesions
MMTV	Mouse mammary tumor viruse
MTs	Microtubules
NIC	NeuNDL2-5-IRES-Cre
NMuMG-Neu-NT	Normal Murin Mammary Gland-Neu-NonTransfected
PEI	Polyethylenimine
TCGA	The Cancer Genome Atlas
TMA	Tumor microarrays
+TIPs	Plus end tracking proteins

DECLARATIONS

Ethics approval and consent to participate

All animal experiments were approved by the Institut de Recherches Cliniques de Montréal Animal Care Committee and were conducted in accordance with the guidelines of the Canadian Council on Animal Care (protocol 2020-14 COT). The use of patient samples for the generation of the tissue microarray (TMA) was approved by the Human Research Ethics Committee of the Centre Hospitalier de l'Université de Montréal (CHUM) under protocol SL 05.019, which authorized the use of these specimens and associated research data.

Consent for publication

All authors have consented to the publication of this article

Competing Interests

The authors declare no competing or financial interests.

Funding

This work was supported by the Cancer Research Society through a partnership with the Rina Primeau Memorial Fund (grant # 23545) and an Excellence Award from the Quebec Breast Cancer Foundation. J.-F.C. holds the Canada Research Chair (Tier-1) in Cellular Signaling and Cancer Metastasis and the Alain Fontaine Chair in Cancer Research from the IRCM Fondation. L.Q. was supported by a doctoral studentship from the Fonds de recherche du Québec-Santé.

Data availability

No large datasets were generated or analyzed during this study. All relevant data supporting the findings of this work are included in the article and its Supplementary Information. Any additional information required to interpret or reproduce the results is available from the corresponding author upon reasonable request.

Author Contributions

Conceptualization: R.C., J.-F.C.; Methodology: R.C., C.M., L.Q., A.R., S.D.; Formal analysis: R.C., C.M., L.Q., A.R., L.G.; Resources: L.G., W.J.M.; Writing-original draft: R.C., J.-F.C.; Writing – review and editing: all authors; Supervision: J.-F.C.

Acknowledgements

We thank all members of the Côté laboratory for helpful discussions and critical reading of the manuscript. We acknowledge the outstanding technical assistance of S. Riverin in the management of mouse colonies and animal procedures. We also recognize the technical support provided by the IRCM Microscopy Facility, the Animal Facility, and the Histology Facility. We thank Dr. M. Cayouette, Dr. S. Meloche, and Dr. A. Fournier for sharing key reagents. We also thank Dr. M. Kmita for access to their M165 FC stereomicroscope.

Authors' information

1. Montreal Clinical Research Institute (IRCM), Montreal, Canada.

2. Department of Anatomy and Cell Biology, McGill University, Montreal, Canada.

3. Molecular Biology Programs, Université de Montréal, Canada.

4. Institute for Research in Immunology and Cancer (IRIC), Montreal, Canada.

5. Goodman Cancer Institute, McGill University, Canada.

6. Department of Medicine, Université de Montréal, Canada.

SUPPLEMENTAL INFORMATION

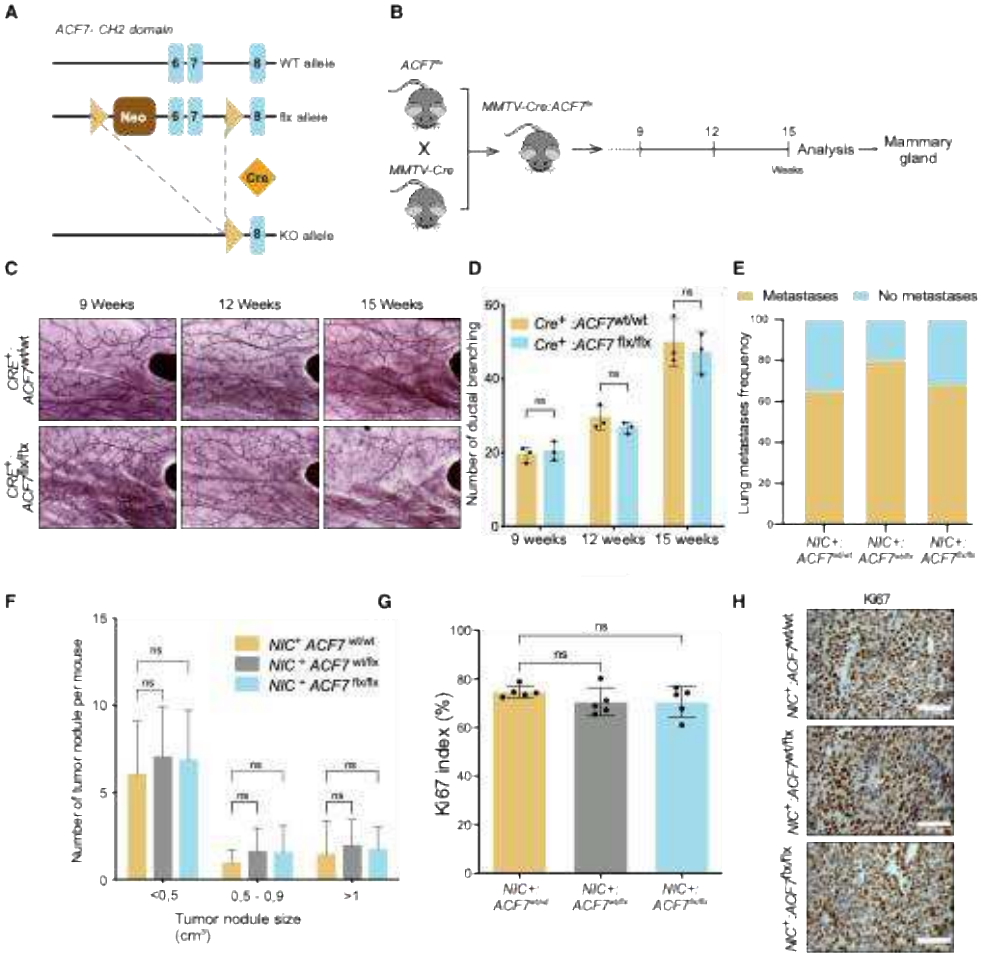


Fig. S1. ACF7 is not involved in the development of mouse mammary gland. A) Strategy used to generate *ACF7*$^{flx/flx}$ mice, adapted from Wu et al., (29), where 6,7 and 8 represents exons, in the CH2 domain of *ACF7*. **B)** Experimental design of the study: *ACF7*$^{flx/flx}$ mice are crossed with *MMTV-Cre* mice to generate *MMTV-Cre*: ACF7^{flx} mice. These mice were sacrificed at 9, 12, and 15 weeks of age, and mammary glands were harvested and stained for quantification. **C)** Whole inguinal mammary gland stained with red carmine at 9, 12, and 15 weeks, allowing the detection of normal ducts and branches in the mice. Scale bar, 1mm. **D)** The graph shows the number of branches at 9, 12, and 15 weeks (n=3 mice per genotype). **E)** Lung metastases frequency across all genotypes (n=22-25). **F)** Distribution of tumor size in cubic centimeters according to the genotype of the mice (n=19-24). **G)** Graph shows the percentage of Ki67-positive cells as a proliferation index (n=5). **H)** Ki67 histological staining showing the proliferative status of the tumors. Scale bar, 50 µm. For **D-F**

and **G**, data are presented as mean ± SD, with statistical analysis performed using one-way ANOVA **(G)** or two-way ANOVA **(D, F)**.

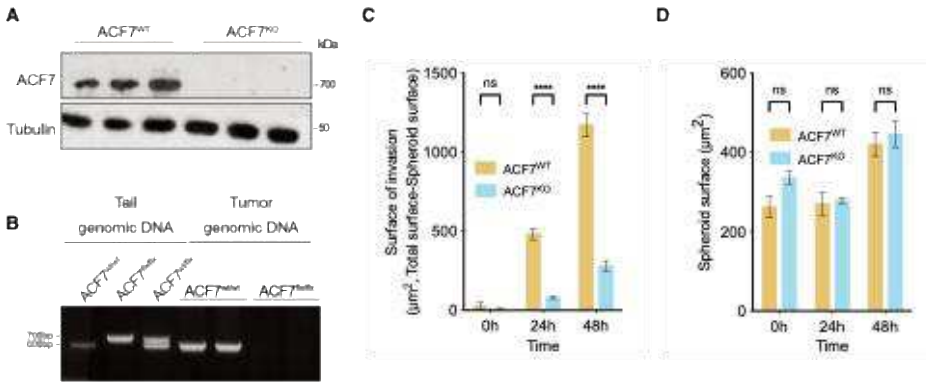


Fig. S2. ACF7 promotes invasion by increasing the number of protrusions per spheroid. A) WB showing the absence of ACF7 proteins in three different ACF7^{KO} primary cell lysates as compared to three control primary cell lines. α-Tubulin is used as loading control. **B)** PCR-based genotyping of mice using DNA extracted from tail tissue and tumor-derived primary cells. **C)** Graph shows the surface of invasion per spheroids at 0, 24 and 48hours. **D)** Graph shows the spheroid surface at 0, 24 and 48hours. The data are presented as mean ± SEM (n=3, N=40 spheroids per genotype), with statistical analysis performed using two-way ANOVA, **** $p < 0.0001$.

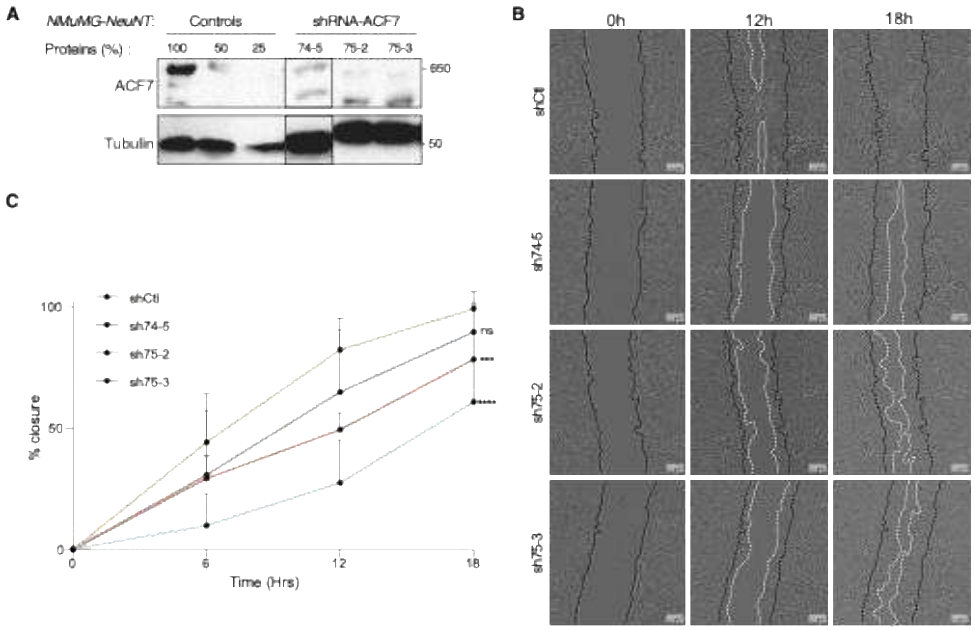
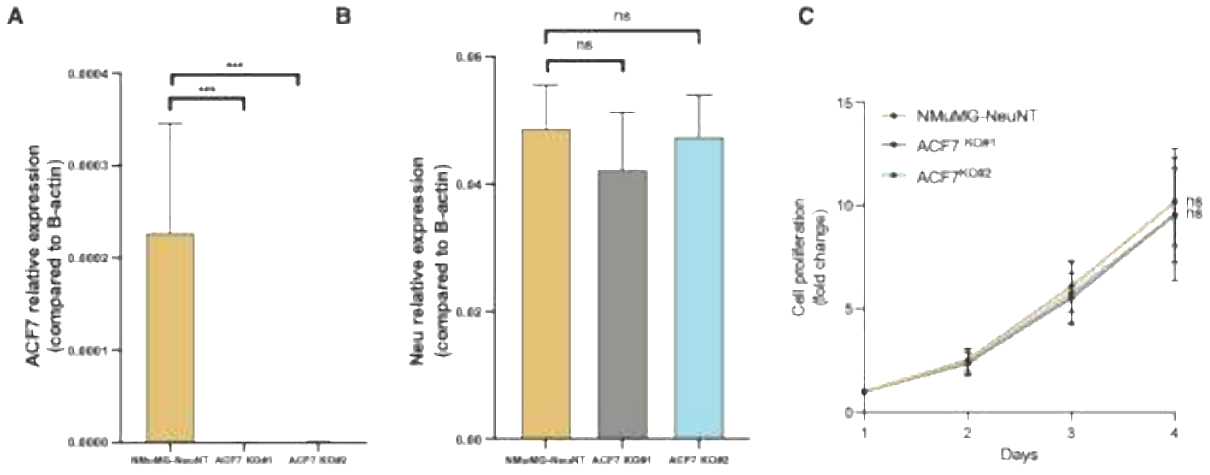


Fig. S3. ACF7 depletion by shRNA reduces migration of NMuMG-NeuNT: ACF7^{KO} cells. A) WB showing ACF7 knock down efficiency of three clones after the use of shRNA against ACF7, with 74 and 75 representing two distinct shRNAs. α-Tubulin is used as loading control. **B)** Images of cell monolayer at indicated time after wound bar: 200 µm. **C)** Graph shows the percentage of wound closure every 6 hours for 24 hours (n=3). Data are presented as mean ± SD, with statistical analysis performed using two-way ANOVA, * p<0,5, ** p<0 01, *** p<0,001, **** p < 0.0001.



762

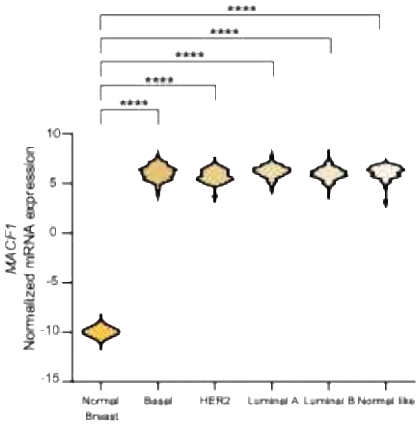
763 **Fig. S4. qPCR analysis of ACF7 expression and assessment of cell proliferation. A-B)** qPCR
764 showing the relative expression of ACF7 (A) and Neu (B) genes as compared to *β-actin* (n=3). **C)**
765 Graph shows the cell proliferation as determined by MTT proliferation assay over 4 days (n=3). The
766 data are presented as mean ± SD, with statistical analysis performed using two-way ANOVA, ***p
767 < 0.0001.

768

A

Sample			N=310
Molecular subtype (%)			
	Luminal A		88 (28,4)
	Luminal B		33 (10,6)
	HER2+		60 (19,4)
	Basal-like		126 (41)
	Normal		3 (1)
MACF1 expression (%)			
	Negative		134 (43,2)
	Low		143 (46,1)
	Medium		21 (6,8)
	High		12 (4)
Follow up	Metastasis		N=129
MACF1 expression			
	Negative		N=53
	Positive		N=76
Metastatic sites (%)			
MACF1 expression			
	Negative	LN	28,3
		Bone	11,3
		Liver	3,77
		Lung	3,77
		Brain	1,88
	Positive	LN	39,47
		Bone	15,78
		Liver	10,52
		Lung	9,21
		Brain	6,57

B



769

770 **Fig. S5. ACF7 mRNA is expressed in all breast cancer subtypes and correlated with poor**
771 **overall survival. A)** Table of patient cohort used for the analysis in Figure 1 A-B-C, N=310 patients.
772 Samples were classified based on breast cancer molecular subtypes (Normal, Basal-like, HER2^{+},
773 Luminal A and Luminal B) and ACF7 IHC score. For analysis of metastatic lesions, the cohort was
774 reduced to N=129 and stratified based on ACF7 IHC score and site of metastasis. **B)** mRNA
775 normalized expression levels of MACF1 across breast cancer subtypes and normal breast tissues

776 from The Cancer Genome Atlas (TCGA). In **B**, data are presented as mean ± SD and statistical

777 analysis performed using one-way ANOVA, ****p < 0.0001.

778

779 **Tables S1 to S5**

780 **Table S1.** List of antibodies and staining reagent

Antibodies	***Purpose***	***Dilution***	***Incubation***	***Catalog #***	***Companies***
Ki-67 (SP6) rabbit monoclonal Ab	IHC	1 :250	O/N, 4°C	275R-15	Cell Marque
Goat Anti-Rabbit IgG Antibody, Biotinylated	IHC	1 :150	1h, RT	BA-100	Vector Laboratories
Streptavidin- HRP	IHC	1 :1000	30 min, RT	554066	BD Pharmigen
MACF1 rabbit polyclonal Ab	WB	1 :10000	O/N, 4°C	A304-564A	Bethyl
TUBA4A (TUBA1) mouse monoclonal Ab	WB / IF	1 :10000 / 1:1000	O/N, 4°C / 1h, RT	T6199	Sigma-Aldrich
ErbB2/HER2 (3B5) mouse monoclonal Ab	WB	1 :5000	O/N, 4°C	sc-33684	Santa Cruz
Acetyl-alpha-Tubulin (Lys40) (D20G3) rabbit monoclonal Ab	WB / IF	1 :1000 / 1:100	O/N, 4°C / 1h, RT	5335	Cell Signaling
β-Actin (ACTB) mouse monoclonal Ab	WB	1 :2000	O/N, 4°C	A5441	Millipore
Goat-Anti-Mouse IgG - HRP	WB	1 :10000	1h, RT	A4416	Sigma
Mouse anti-rabbit IgG - HRP	WB	1 :10000	1h, RT	sc-2357	Santa Cruz
Paxillin mouse monoclonal Ab	IF	1 : 400	1h, RT	612405	BD-Biosciences
Alexa Fluor™ 488 Chicken anti-Mouse IgG	IF	1 :500	1h, RT	A21200	Invitrogen
Alexa Fluor™ 568Goat anti-Mouse IgG	IF	1 :500	1h, RT	A11031	Invitrogen
Alexa Fluor™ 488 phalloidin	IF	1 :100	1h, RT	A12379	Invitrogen
Alexa Fluor™ 568 phalloidin	IF	1 :500	1h, RT	A12380	Invitrogen
Alexa Fluor™ 633 phalloidin	IF	1 :500	1h, RT	A22284	Invitrogen
Hoechst 33342, trihydrochloride trihydrate	IF	1 :10000	10 min, RT	H3570	Invitrogen

781

782

783

784

785 **Table S2.** Plasmids used in this study

Plasmids	***Companies***
PL-EGFP-C1	Gifted by Dr. Cayouette
pCl-ampho	Gifted by Dr. Meloche
EB3-GFP	Gifted by Dr. Fournier
PL-EB3-EGFP	Generated in this study
pMD2.G	Addgene #12259
pLKO.1-puro-shRNA-Control (Clone Number TRCN0000125614)	Sigma-Aldrich
pLKO.1-puro-shRNA-ACF7-Murine #74 (Clone NumberTRCN0000089574)	Sigma-Aldrich
pLKO.1-puro-shRNA-ACF7-Murine #75 (Clone NumberTRCN0000089575)	Sigma-Aldrich
pRSV-Rev	Addgene #12253
pMDLg/pREE	Addgene #12251
pMD2-VSVG	Addgene #12259
pLentiCRISPRv2	Addgene #52961
pLentiCRISPRv2-mACF7-2	Generated in this study
pLentiCRISPRv2-mACF7-9	Generated in this study
pLentiCRISPRv2-mACF7-29	Generated in this study

786

787 **Table S3.** List of shRNA sequences

shRNA	***Sequence***
shRNA-Control	CCGGGCGCGATAGCGCTAATAATTTCTC-GAGAAATTATTAGCGCTATCGCGCTTTTT
shRNA-74	CCTGAGATCATCCAAGAATTT
shRNA-75	CCAGTGAGATTCGGTCTGATT

788

789 **Table S4.** List of primers used in this study

Primer	**Sequence (5' – 3')**	***Purpose***
Acf7 Forward	GCTTCAGCCGCCGCC	qPCR
Acf7 Reverse	TGGCTACAGGAAGGACCAGA	qPCR

β-actin Forward	TGATGGTGGGAATGGGTCAGAA	qPCR
β-actin Reverse	TCCATGTCGTCCCAGTTGGTAA	qPCR
mERBB2 Forward	GGCACTGTCTACAAGGGCAT	qPCR
mERBB2 Reverse	GAGGCGGGACACATATGGAG	qPCR
ACF7 Forward	AAA GAA ACG GAA ATA CTG GCC	Genotyping
ACF7 Reverse	GCA GCT TAA TTC TGC CAA ATT C	Genotyping
ErbB2 Forward	TTC CGG AAC CCA CAT CAG GCC	Genotyping
ErbB2 Reverse	GTT TCC TGC AGC AGC CTA CGC	Genotyping
Cre Transgene Forward	GCG GTC TGG CAG TAA AAA CTA TC	Genotyping
Cre Transgene Reverse	GTG AAA CAG CAT TGC TGT CAC TT	Genotyping
Cre Control Forward	CTA GGC CAC AGA ATT GAA AGA TCT	Genotyping
Cre Control Reverse	GTA GGT GGA AAT TCT AGC ATC ATC C	Genotyping

Table S5. List of guide RNA sequences

guideRNA	***Sequence (5' – 3')***
mACF7-2. Forward	caccgGGTTTCGAAAACCGATGACCCGG
mACF7-2. Reverse	aaacCCGGGTCATCGGTTTTCGAAACCc
mACF7-9. Forward	caccgGGTCATCGGTTTTCGAAACCAGG
mACF7-9. Reverse	aaacCCTGGTTTCGAAAACCGATGACCc
mACF7-29. Forward	caccgCAGGCCCGATCTGGTAGACATGG
mACF7-29. Reverse	aaacCCATGTCTACCAGATCGGGCCTGc

Adaptors are in lowercase while guide RNAs are written in uppercase.

Legends for Movies S1 to S5

Movie S1 (separate file). Live cell imaging of random cell migration of ACF7^{WT} (left) and ACF7^{KO} cells tracked every hour during 24hours. Scale bar: 100 µm. Related to Figure 2.

Movie S2 (separate file). Live cell imaging of wound healing of ACF7^{WT} (left) and ACF7^{KO} cells tracked every hour during 24hours. Scale bar: 100 µm. Related to Figure 2.

Movie S3 (separate file). Live cell imaging of EB3-EGFP dynamic in ACF7^{WT} (left) and ACF7^{KO} cells tracked every 10 seconds for 2 minutes. Scale bar: 10 µm. Related to Figure 3.

Movie S4 (separate file). Live cell imaging of wound healing of NMuMG-NeuNt-shCtl (top left), NMuMG-NeuNt-sh74-5 (top right), NMuMG-NeuNt-sh75-2 (bottom left) and NMuMG-NeuNt-sh75-3 (bottom right) cells tracked every hour during 24hours. Scale bar: 100 µm. Related to Fig S3.

Movie S5 (separate file). Live cell imaging of wound healing of NMuMG-NeuNT (left), ACF7$^{KO\#1}$ (middle) and ACF7$^{KO\#2}$ cells tracked every hour during 24hours. Scale bar: 100 µm. Related to Figure 4.

REFERENCES

1. Sung H, Ferlay J, Siegel RL, Laversanne M, Soerjomataram I, Jemal A, et al. Global Cancer Statistics 2020: GLOBOCAN Estimates of Incidence and Mortality Worldwide for 36 Cancers in 185 Countries. CA Cancer J Clin. 2021;71(3):209-49.
2. Slamon DJ, Clark GM, Wong SG, Levin WJ, Ullrich A, McGuire WL. Human breast cancer: correlation of relapse and survival with amplification of the HER-2/neu oncogene. Science. 1987;235(4785):177-82.
3. Perou CM, Sorlie T, Eisen MB, van de Rijn M, Jeffrey SS, Rees CA, et al. Molecular portraits of human breast tumours. Nature. 2000;406(6797):747-52.
4. Wolff AC, Hammond MEH, Allison KH, Harvey BE, Mangu PB, Bartlett JMS, et al. Human Epidermal Growth Factor Receptor 2 Testing in Breast Cancer: American Society of Clinical Oncology/College of American Pathologists Clinical Practice Guideline Focused Update. J Clin Oncol. 2018;36(20):2105-22.
5. Swain SM, Baselga J, Kim SB, Ro J, Semiglazov V, Campone M, et al. Pertuzumab, Trastuzumab, and Docetaxel in HER2-Positive Metastatic Breast Cancer. New Engl J Med. 2015;372(8):724-34.
6. Loibl S, Gianni L. HER2-positive breast cancer. Lancet. 2017;389(10087):2415-29.
7. Swain SM, Shastry M, Hamilton E. Targeting HER2-positive breast cancer: advances and future directions. Nat Rev Drug Discov. 2023;22(2):101-26.

8. Nahta R, Yu D, Hung MC, Hortobagyi GN, Esteva FJ. Mechanisms of disease: understanding resistance to HER2-targeted therapy in human breast cancer. Nat Clin Pract Oncol. 2006;3(5):269-80.
9. Rexer BN, Arteaga CL. Intrinsic and acquired resistance to HER2-targeted therapies in HER2 gene-amplified breast cancer: mechanisms and clinical implications. Crit Rev Oncog. 2012;17(1):1-16.
10. Pohlmann PR, Mayer IA, Mernaugh R. Resistance to Trastuzumab in Breast Cancer. Clin Cancer Res. 2009;15(24):7479-91.
11. Chaffer CL, Weinberg RA. A perspective on cancer cell metastasis. Science. 2011;331(6024):1559-64.
12. Steeg PS. Targeting metastasis. Nat Rev Cancer. 2016;16(4):201-18.
13. Luzzi KJ, MacDonald IC, Schmidt EE, Kerkvliet N, Morris VL, Chambers AF, et al. Multistep nature of metastatic inefficiency: dormancy of solitary cells after successful extravasation and limited survival of early micrometastases. Am J Pathol. 1998;153(3):865-73.
14. Lambert AW, Pattabiraman DR, Weinberg RA. Emerging Biological Principles of Metastasis. Cell. 2017;168(4):670-91.
15. Elkholi IE, Lalonde A, Park M, Cote JF. Breast Cancer Metastatic Dormancy and Relapse: An Enigma of Microenvironment(s). Cancer Res. 2022;82(24):4497-510.
16. Aguirre-Ghiso JA. Models, mechanisms and clinical evidence for cancer dormancy. Nat Rev Cancer. 2007;7(11):834-46.
17. Massague J, Obenauf AC. Metastatic colonization by circulating tumour cells. Nature. 2016;529(7586):298-306.
18. Thiery JP, Acloque H, Huang RY, Nieto MA. Epithelial-mesenchymal transitions in development and disease. Cell. 2009;139(5):871-90.
19. Nieto MA, Huang RY, Jackson RA, Thiery JP. Emt: 2016. Cell. 2016;166(1):21-45.
20. Pollard TD, Borisy GG. Cellular motility driven by assembly and disassembly of actin filaments. Cell. 2003;112(4):453-65.
21. Ridley AJ, Schwartz MA, Burridge K, Firtel RA, Ginsberg MH, Borisy G, et al. Cell migration: integrating signals from front to back. Science. 2003;302(5651):1704-9.
22. Alonso-Matilla R, Provenzano PP, Odde DJ. Physical principles and mechanisms of cell migration. NPJ Biol Phys Mech. 2025;2(1):2.
23. Stehbens S, Wittmann T. Targeting and transport: how microtubules control focal adhesion dynamics. J Cell Biol. 2012;198(4):481-9.
24. Seetharaman S, Etienne-Manneville S. Microtubules at focal adhesions - a double-edged sword. J Cell Sci. 2019;132(19).
25. Stehbens SJ, Paszek M, Pemble H, Ettinger A, Gierke S, Wittmann T. CLASPs link focal-adhesion-associated microtubule capture to localized exocytosis and adhesion site turnover. Nat Cell Biol. 2014;16(6):561-73.
26. Kaverina I, Krylyshkina O, Small JV. Microtubule targeting of substrate contacts promotes their relaxation and dissociation. J Cell Biol. 1999;146(5):1033-44.
27. Rodriguez OC, Schaefer AW, Mandato CA, Forscher P, Bement WM, Waterman-Storer CM. Conserved microtubule-actin interactions in cell movement and morphogenesis. Nat Cell Biol. 2003;5(7):599-609.
28. Waterman-Storer CM, Worthylake RA, Liu BP, Burridge K, Salmon ED. Microtubule growth activates Rac1 to promote lamellipodial protrusion in fibroblasts. Nat Cell Biol. 1999;1(1):45-50.
29. Wu X, Kodama A, Fuchs E. ACF7 regulates cytoskeletal-focal adhesion dynamics and migration and has ATPase activity. Cell. 2008;135(1):137-48.

30. Kodama A, Karakesisoglou I, Wong E, Vaezi A, Fuchs E. ACF7: an essential integrator of microtubule dynamics. Cell. 2003;115(3):343-54.
31. Suozzi KC, Wu X, Fuchs E. Spectraplakins: master orchestrators of cytoskeletal dynamics. J Cell Biol. 2012;197(4):465-75.
32. Leung CL, Sun D, Zheng M, Knowles DR, Liem RK. Microtubule actin cross-linking factor (MACF): a hybrid of dystonin and dystrophin that can interact with the actin and microtubule cytoskeletons. J Cell Biol. 1999;147(6):1275-86.
33. Cusseddu R, Robert A, Cote JF. Strength Through Unity: The Power of the Mega-Scaffold MACF1. Front Cell Dev Biol. 2021;9:641727.
34. Margaron Y, Fradet N, Cote JF. ELMO recruits actin cross-linking family 7 (ACF7) at the cell membrane for microtubule capture and stabilization of cellular protrusions. J Biol Chem. 2013;288(2):1184-99.
35. Duhamel S, Goyette MA, Thibault MP, Filion D, Gaboury L, Cote JF. The E3 Ubiquitin Ligase HectD1 Suppresses EMT and Metastasis by Targeting the +TIP ACF7 for Degradation. Cell Rep. 2018;22(4):1016-30.
36. Wu X, Shen QT, Oristian DS, Lu CP, Zheng Q, Wang HW, et al. Skin stem cells orchestrate directional migration by regulating microtubule-ACF7 connections through GSK3beta. Cell. 2011;144(3):341-52.
37. Chen HJ, Lin CM, Lin CS, Perez-Olle R, Leung CL, Liem RK. The role of microtubule actin cross-linking factor 1 (MACF1) in the Wnt signaling pathway. Genes Dev. 2006;20(14):1933-45.
38. Marone R, Hess D, Dankort D, Muller WJ, Hynes NE, Badache A. Memo mediates ErbB2-driven cell motility. Nat Cell Biol. 2004;6(6):515-22.
39. Zaoui K, Honore S, Isnardon D, Braguer D, Badache A. Memo-RhoA-mDia1 signaling controls microtubules, the actin network, and adhesion site formation in migrating cells. J Cell Biol. 2008;183(3):401-8.
40. Zaoui K, Benseddik K, Daou P, Salaun D, Badache A. ErbB2 receptor controls microtubule capture by recruiting ACF7 to the plasma membrane of migrating cells. Proc Natl Acad Sci U S A. 2010;107(43):18517-22.
41. Ursini-Siegel J, Hardy WR, Zuo DM, Lam SH, Sanguin-Gendreau V, Cardiff RD, et al. ShcA signalling is essential for tumour progression in mouse models of human breast cancer. Embo J. 2008;27(6):910-20.
42. Andrechek ER, Hardy WR, Siegel PM, Rudnicki MA, Cardiff RD, Muller WJ. Amplification of the neu/erbB-2 oncogene in a mouse model of mammary tumorigenesis. Proc Natl Acad Sci U S A. 2000;97(7):3444-9.
43. Laurin M, Huber J, Pelletier A, Houalla T, Park M, Fukui Y, et al. Rac-specific guanine nucleotide exchange factor DOCK1 is a critical regulator of HER2-mediated breast cancer metastasis. P Natl Acad Sci USA. 2013;110(18):7434-9.
44. Brantley-Sieders DM, Zhuang G, Hicks D, Fang WB, Hwang Y, Cates JM, et al. The receptor tyrosine kinase EphA2 promotes mammary adenocarcinoma tumorigenesis and metastatic progression in mice by amplifying ErbB2 signaling. J Clin Invest. 2008;118(1):64-78.
45. Shalem O, Sanjana NE, Hartenian E, Shi X, Scott DA, Mikkelson T, et al. Genome-scale CRISPR-Cas9 knockout screening in human cells. Science. 2014;343(6166):84-7.
46. Sanjana NE, Shalem O, Zhang F. Improved vectors and genome-wide libraries for CRISPR screening. Nat Methods. 2014;11(8):783-4.
47. Yousef EM, Tahir MR, St-Pierre Y, Gaboury LA. MMP-9 expression varies according to molecular subtypes of breast cancer. BMC Cancer. 2014;14:609.
48. Wolff AC, Hammond ME, Hicks DG, Dowsett M, McShane LM, Allison KH, et al. Recommendations for human epidermal growth factor receptor 2 testing in breast cancer:

American Society of Clinical Oncology/College of American Pathologists clinical practice guideline update. Arch Pathol Lab Med. 2014;138(2):241-56.
49. Bai XF, Ni XG, Zhao P, Liu SM, Wang HX, Guo B, et al. Overexpression of annexin 1 in pancreatic cancer and its clinical significance. World J Gastroenterol. 2004;10(10):1466-70.
50. Chen HM, MacDonald JA. Network analysis of TCGA and GTEx gene expression datasets for identification of trait-associated biomarkers in human cancer. STAR Protoc. 2022;3(1):101168.
51. Cerami E, Gao J, Dogrusoz U, Gross BE, Sumer SO, Aksoy BA, et al. The cBio cancer genomics portal: an open platform for exploring multidimensional cancer genomics data. Cancer Discov. 2012;2(5):401-4.
52. Gao J, Aksoy BA, Dogrusoz U, Dresdner G, Gross B, Sumer SO, et al. Integrative analysis of complex cancer genomics and clinical profiles using the cBioPortal. Sci Signal. 2013;6(269):pl1.
53. de Bruijn I, Kundra R, Mastrogiacomo B, Tran TN, Sikina L, Mazor T, et al. Analysis and Visualization of Longitudinal Genomic and Clinical Data from the AACR Project GENIE Biopharma Collaborative in cBioPortal. Cancer Res. 2023;83(23):3861-7.
54. Herschkowitz JI, Simin K, Weigman VJ, Mikaelian I, Usary J, Hu Z, et al. Identification of conserved gene expression features between murine mammary carcinoma models and human breast tumors. Genome Biol. 2007;8(5):R76.
55. Kaminska M, Ciszewski T, Lopacka-Szatan K, Miotla P, Staroslawska E. Breast cancer risk factors. Prz Menopauzalny. 2015;14(3):196-202.
56. Nagano M, Hoshino D, Koshikawa N, Akizawa T, Seiki M. Turnover of focal adhesions and cancer cell migration. Int J Cell Biol. 2012;2012:310616.
57. Eshun-Wilson L, Zhang R, Portran D, Nachury MV, Toso DB, Lohr T, et al. Effects of alpha-tubulin acetylation on microtubule structure and stability. Proc Natl Acad Sci U S A. 2019;116(21):10366-71.
58. Di Martile M, Del Bufalo D, Trisciuoglio D. The multifaceted role of lysine acetylation in cancer: prognostic biomarker and therapeutic target. Oncotarget. 2016;7(34):55789-810.
59. Boggs AE, Vitolo MI, Whipple RA, Charpentier MS, Goloubeva OG, Ioffe OB, et al. alpha-Tubulin acetylation elevated in metastatic and basal-like breast cancer cells promotes microtentacle formation, adhesion, and invasive migration. Cancer Res. 2015;75(1):203-15.
60. Mohan R, Katrukha EA, Doodhi H, Smal I, Meijering E, Kapitein LC, et al. End-binding proteins sensitize microtubules to the action of microtubule-targeting agents. Proc Natl Acad Sci U S A. 2013;110(22):8900-5.
61. Laurin M, Fradet N, Blangy A, Hall A, Vuori K, Cote JF. The atypical Rac activator Dock180 (Dock1) regulates myoblast fusion in vivo. Proc Natl Acad Sci U S A. 2008;105(40):15446-51.
62. Akhmanova A, Steinmetz MO. Control of microtubule organization and dynamics: two ends in the limelight. Nat Rev Mol Cell Biol. 2015;16(12):711-26.